

Toward improved regional hydrological model performance using a novel soil data-informed calibration method

Chuxuan Li¹, Guo Yu², Jiali Wang³, and Daniel E Horton¹

¹Northwestern University

²Desert Research Institute

³Argonne National Laboratory (DOE)

January 11, 2023

Abstract

Accurate soil moisture and streamflow data are an aspirational need of many hydrologically-relevant fields. Model simulated soil moisture and streamflow hold promise but numerical models require calibration prior to application to ensure sufficient model performance. Manual or automated calibration methods require iterative model runs and hence are computationally expensive. In this study, we leverage the Soil Survey Geographic (SSURGO) database and the probability mapping of SSURGO (POLARIS) to help constrain soil parameter uncertainties in the Weather Research and Forecasting Hydrological modeling system (WRF-Hydro) over a central California domain. After calibration, WRF-Hydro soil moisture exhibits increased correlation coefficients (r), reduced biases, and increased Kling-Gupta Efficiencies (KGEs) across seven in-situ soil moisture observing stations. Compared to four well-established soil moisture datasets including Soil Moisture Active Passive Level 4 data and three Phase 2 North American Land Data Assimilation System land surface models, our POLARIS-calibrated WRF-Hydro produces the highest mean KGE (0.67) across the seven stations. More importantly, WRF-Hydro streamflow fidelity also increases especially in the case where the model domain is set up with an SSURGO-informed total soil thickness. Both the magnitude and timing of peak flow events are better captured, r increases across nine United States Geological Survey stream gages, and the mean Nash-Sutcliffe Efficiency across seven of the nine gages increases from 0.19 in default WRF-Hydro to 0.63 after calibration. Our soil data-informed calibration approach, which is transferable to other spatially-distributed hydrological models, uses open-access data and non-iterative steps to improve model performance and is thus operationally and computationally attractive.

Hosted file

953402_0_art_file_10582675_rnxm11.docx available at <https://authorea.com/users/559535/articles/618234-toward-improved-regional-hydrological-model-performance-using-a-novel-soil-data-informed-calibration-method>

Hosted file

953402_0_supp_10582588_rnxzxxk.docx available at <https://authorea.com/users/559535/articles/618234-toward-improved-regional-hydrological-model-performance-using-a-novel-soil-data-informed-calibration-method>

1 **Toward improved regional hydrological model performance using a novel soil data-informed
2 calibration method**

3 Chuxuan Li¹, Guo Yu², Jiali Wang³, and Daniel E. Horton¹

4 1. Department of Earth and Planetary Sciences, Northwestern University, Evanston, IL 60208, USA

5 2. Division of Hydrologic Sciences, Desert Research Institute, Las Vegas, NV, 89119, USA

6 3. Environmental Science Division, Argonne National Laboratory, Lemont, IL, 60439, USA

7

8 **Key points:**

- 9 • Model simulated soil moisture and streamflow fidelity substantially improve by using
10 computationally-efficient soil data-based calibration.
- 11 • Calibrated surface soil moisture outperforms four well-established soil moisture products when
12 evaluated against in situ observations.
- 13 • After calibration, the model's capability to simulate observed streamflow hydrographs improves,
14 especially peak flow fidelity.

15

16 **Abstract:**

17 Accurate soil moisture and streamflow data are an aspirational need of many hydrologically-relevant
18 fields. Model simulated soil moisture and streamflow hold promise but numerical models require
19 calibration prior to application to ensure sufficient model performance. Manual or automated calibration
20 methods require iterative model runs and hence are computationally expensive. In this study, we leverage
21 the Soil Survey Geographic (SSURGO) database and the probability mapping of SSURGO (POLARIS)
22 to help constrain soil parameter uncertainties in the Weather Research and Forecasting Hydrological
23 modeling system (WRF-Hydro) over a central California domain. After calibration, WRF-Hydro soil
24 moisture exhibits increased correlation coefficients (r), reduced biases, and increased Kling-Gupta
25 Efficiencies (KGEs) across seven in-situ soil moisture observing stations. Compared to four well-
26 established soil moisture datasets including Soil Moisture Active Passive Level 4 data and three Phase 2
27 North American Land Data Assimilation System land surface models, our POLARIS-calibrated WRF-
28 Hydro produces the highest mean KGE (0.67) across the seven stations. More importantly, WRF-Hydro
29 streamflow fidelity also increases especially in the case where the model domain is set up with an
30 SSURGO-informed total soil thickness. Both the magnitude and timing of peak flow events are better
31 captured, r increases across nine United States Geological Survey stream gages, and the mean Nash-

32 Sutcliffe Efficiency across seven of the nine gages increases from 0.19 in default WRF-Hydro to 0.63
33 after calibration. Our soil data-informed calibration approach, which is transferable to other spatially-
34 distributed hydrological models, uses open-access data and non-iterative steps to improve model
35 performance and is thus operationally and computationally attractive.

36 **Key words:** soil moisture, streamflow, data-informed calibration, hydrological models

37

38 **Plain language summary**

39 In this study, we develop a method that uses field- and machine learning-derived soil property
40 uncertainties to improve the performance of a hydrological model to simulate observed soil water content
41 and river flows. Specifically, we replace three of the model's default parameters with the corresponding
42 parameters from a probabilistic soil property dataset. After replacement, simulated soil water content
43 more closely resembles observations from seven in-situ observing stations. Compared to four other well-
44 established, satellite-derived and model-simulated products, our soil property-calibrated model performs
45 favorably. For river flows, we find the highest model performance in the case where we modify the total
46 soil thickness according to the soil survey dataset. With modified soil thickness, the timing and magnitude
47 of high flows are much better captured and the similarity between our simulations and the observations
48 substantially increases at almost all observing stations. Compared to calibration methods that require
49 repetitive model runs, our probabilistic soil property calibration method is computationally-efficient and
50 may prove useful in a number of hydrologic modeling contexts.

51

52 **1. Introduction**

53 Soil moisture and streamflow are two key components of the hydrologic cycle. In the following, we
54 provide examples to show their importance for a plethora of fields including hydrology, geomorphology,
55 natural hazards, ecology, water resource management, and climate science. For natural hazards and
56 geomorphology, both soil moisture and streamflow can influence the likelihood of flooding (Koster et al.
57 2010; Massari et al. 2014) and debris flows (Coe et al. 2008; Kean et al. 2013; Tang et al. 2019), while
58 soil moisture has also been used to predict drought (Xu et al. 2020) and shallow landslides (Gasmo et al.
59 2000; Handwerger et al. 2019; Johnson and Sitar 1990; Ray and Jacobs 2007; Sweeney and Robertson
60 1979). In water supply management, soil moisture influences forest water yield and streamflow controls
61 suspended sediment transport and water quality (Acharya et al. 2022; Colby 1956). Water in soil and river
62 channels also drives the productivity and sustainability of terrestrial ecosystems, especially in arid and

63 semi-arid regions (Legates et al. 2011), influencing crop yields and other aspects of agriculture (Berg and
64 Sheffield 2018; Carrão et al. 2016; Kang et al. 2009). Over climatic timescales, soil moisture affects both
65 short- and long-term climate by modulating the hydro-climate feedback loop (Seneviratne et al. 2010;
66 Seneviratne et al. 2013; Yeh et al. 1984). Because soil moisture and streamflow play important roles in
67 the broad Earth system across various spatiotemporal scales, accurate estimates of them are critical to
68 improve the predictive skills of models in a wide range of fields. For example, initializing models with
69 realistic soil moisture can reduce uncertainties in atmospheric predictions at sub-seasonal to seasonal
70 scales in climate models (Douville and Chauvin 2000; Fennelly and Shukla 1999; Koster 2004) and
71 facilitate accurate landslide predictions in slope stability models (Cai et al. 2019; Di Matteo et al. 2018).
72 On climatic timescales, soil moisture can greatly impact projections of extreme temperature and
73 precipitation in global climate models (Seneviratne et al. 2013). In ecological and agricultural models,
74 soil moisture is needed to simulate carbon cycles (Friend and Kiang 2005; Yuste et al. 2007) and crop
75 growth (Rosenzweig et al. 2002) and is a key variable for predicting agricultural drought (Crow et al.
76 2012; Narasimhan and Srinivasan 2005). Streamflow is also an indispensable variable used in
77 hydrological hazard mapping and assessment tools, water resource management tools, landscape
78 evolution models, and coupled atmospheric-hydrological models (Davy and Lague 2009; Dottori et al.
79 2016; Gong et al. 2010; Wagner et al. 2016).

80 In-situ observations of soil moisture and streamflow are regarded as ground truth. However, they are
81 spatially sparse due to the high costs of large-scale implementation especially in remote and
82 topographically complex regions. This is especially a problem for obtaining in-situ soil moisture
83 observations. Satellites using passive microwave techniques such as Soil Moisture Active Passive
84 (SMAP), on the other hand, provide promising remotely-sensed surface soil moisture with global data
85 coverage (Al-Yaari et al. 2017; Chen et al. 2018; Kumar et al. 2018). However, satellite-derived data is
86 reported to be biased in heavily vegetated areas (Fan et al. 2020; Ma et al. 2019; Reichle et al. 2017) and
87 is subject to data gaps primarily due to satellite orbits (Tavakol et al. 2019; Wang et al. 2012). In addition,
88 remote sensing techniques can only retrieve skin (0–5 cm) or near-surface soil moisture (Mohanty et al.
89 2017). As such, process-based land surface models (LSMs) are frequently used to fill the data gaps in
90 satellite-derived soil moisture and extend soil moisture estimates to the root zone (~1–2 m below ground)
91 (Koster et al. 2009; Mohanty et al. 2017; Tavakol et al. 2019). However, LSMs at global or regional
92 scales often have rather coarse resolutions (e.g., 1/8 degree in NLDAS-2 LSMs). Due to the high
93 variability in soil moisture across space and time, efforts to produce high-resolution soil moisture are
94 needed for both regional-scale and locally-focused applications.

Physics-based hydrological models that simulate soil moisture and streamflow at high resolutions are critical tools to fill in-situ and remotely-sensed gaps but models need validation prior to application. Improving hydrological models' soil moisture and streamflow performance has been a long-standing research objective. In these models, soil moisture and streamflow are prognostic variables that are often subject to great uncertainties originating from various sources including model physics and structure, meteorological forcing, and parameterizations (Leach et al. 2018; Matgen et al. 2010; Silver et al. 2017). To improve simulation fidelity, a number of different techniques have been employed including data assimilation and manual or automated calibration. So far, data assimilation has been the primary technique to improve soil moisture simulations in hydrological models and it has shown promising results by incorporating remotely-sensed soil moisture data (Crow and Van den Berg 2010; De Santis et al. 2021; Loizu et al. 2018). It is also found that assimilating observational soil moisture can improve the accuracy of both soil moisture and streamflow predictions in various types of models (Aubert et al. 2003; Lee et al. 2011). Assimilating observational streamflow and/or snow data is also applied to improve streamflow simulations (Lahmers et al. 2022) and forecasts (Boucher et al. 2020). Despite its successful applications, data assimilation typically requires a large volume of high-quality observational data which are often not available in data-scarce regions. Other efforts to improve model predictions include model calibration. Typically, hydrological models are calibrated either manually (i.e., via a trial-and-error process (Yucel et al. 2015)) or using an automated algorithm (Becker et al. 2019; Gallagher et al. 2007). Both manual and automated-algorithm-based calibration techniques require iterative model runs to arrive at the optimal combination of parameters. Even though parallelization has saved considerable computing hours (Alvioli et al. 2016; Baum et al. 2008; Wang et al. 2019), this calibration process could still be complicated and resource-demanding, especially when the model domain is large and spatial resolution is high.

Here, we develop a soil property data-informed calibration method to calibrate both soil moisture and streamflow simulations with non-iterative steps in the Weather Research and Forecasting Hydrological modeling system version 5.1.1 (WRF-Hydro; Gochis et al. 2020). WRF-Hydro is a 3-D, fully-distributed, and physics-based open-source community hydrological model. Compared with other traditional hydrological models such as the semi-distributed Variable Infiltration Capacity model (VIC), WRF-Hydro is a fully-distributed model that considers spatially distributed hydrological variables (Yin et al. 2020); compared with the quasi-physically-based Soil and Water Assessment Tool (SWAT) that works at single watershed- to river basin-scales, WRF-Hydro can simulate multi-processes across multiple scales. In operational mode, WRF-Hydro works as the hydrologic core of National Water Model (NWM) to produce streamflow predictions at ~2.7 million river reaches. In research settings, streamflow from WRF-Hydro has been calibrated manually (Yucel et al. 2015) or using automatic algorithms (Lahmers et al. 2020; Lahmers et al. 2019; Wang et al. 2019; Yu et al. 2020). Sofokleous et al. (2022) found streamflow

129 predictions in WRF-Hydro are improved with improved representation of groundwater and transpiration
130 processes, which highlights the importance of replicating the real-world conditions with realistic
131 parameters as opposed to intensively calibrating the parameters. In that respect, in contrast to manual and
132 auto-algorithm-based calibration studies, Silver et al. (2017) outlined a systematic calibration procedure
133 that employs physical soil characteristics derived from remote sensing to calibrate streamflow in WRF-
134 Hydro. However, similar calibration methods have not been applied to soil moisture in WRF-Hydro and
135 the use of soil moisture from WRF-Hydro simulations has thus far been limited. In addition, it is not clear
136 whether the improved soil moisture can improve streamflow simulation as well in WRF-Hydro. Therefore,
137 to simplify the calibration procedure and increase the utility of high-resolution soil moisture simulation in
138 WRF-Hydro, here we develop a calibration approach that relies on two related open-access soil databases
139 i.e., SSURGO and Probability Mapping of Soil Survey Geographic Database (POLARIS; Chaney et al.
140 2016). Our calibrated experiments show improved simulation-observation fidelity for both soil moisture
141 and streamflow. With the improvement, our approach may increase the utility of WRF-Hydro and
142 potentially other spatially-distributed hydrological models for a number of hydrologically relevant fields,
143 including climate science, natural hazards, agriculture, and ecology. In the following, our study domain
144 and environmental setting are introduced in Section 2, descriptions of the model, data, and the data-
145 informed calibration method are presented in Section 3, Section 4 presents the results, and Section 5
146 provides discussions and a conclusion.

147

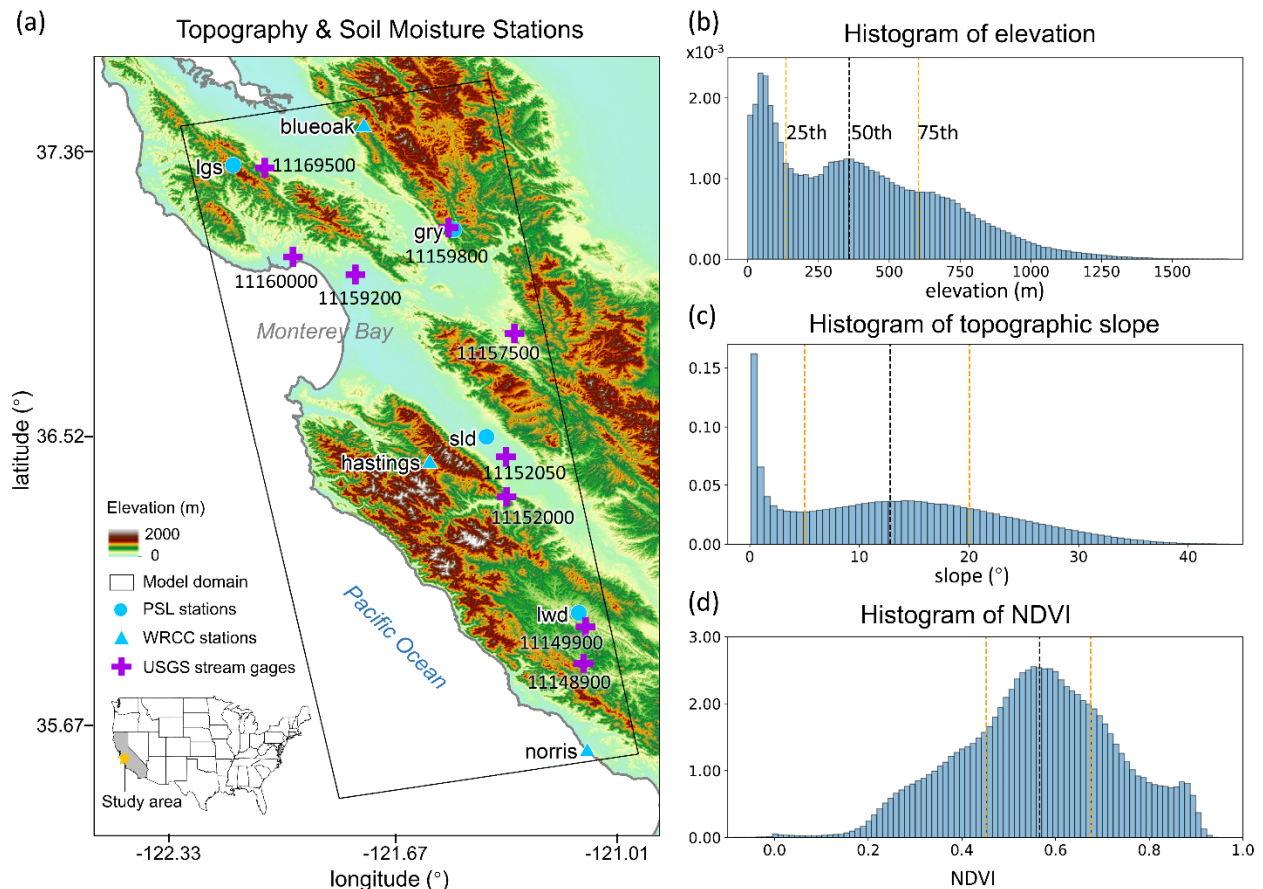
148 **2. Study area and environmental setting**

149 Our study area is located in the Coast Ranges surrounding Monterey Bay in central California, USA
150 (Fig. 1a). The WRF-Hydro model domain outlined by the black box in Fig. 1a covers several
151 mountainous areas, seven in-situ soil moisture stations, and nine United States Geological Survey (USGS)
152 stream gages. Soil moisture stations Los Gatos (lgs), Gilroy (gry), Soledad (sld), and Lockwood (lwd) are
153 operated by the NOAA Physical Sciences Laboratory (PSL), whereas stations blueoak, norris, and
154 hastings are operated by the Western Regional Climate Center (WRCC). The streamflow measured at the
155 nine USGS stream gages are natural flows (i.e., flows without human regulations). The details regarding
156 the soil moisture and streamflow observational sites are given in Section 3.4.1. California has a
157 Mediterranean climate with distinct wet and dry seasons. About 80% of annual precipitation in California
158 falls within the wet season [defined as November to April in Jong et al. (2016)]. Due to the Mediterranean
159 climate, soil moisture in California also has high seasonal variability, similar to precipitation.

160 Our model domain features complex topography and heterogeneous vegetation cover (Fig.1b-d). The
161 histograms of elevation and slope are calculated based on USGS National Elevation Dataset (NED) 30-m

162 Digital Elevation Model (DEM). Both distributions have a bimodal shape i.e., the majority of the model
 163 domain has topographic elevations 30-40 m above sea level and minimal slopes, and the secondary peaks
 164 in the distributions, however, correspond to topographic elevations of 300 m and slopes of 13°. The
 165 interquartile range of topographic slope spans more than 15°, showing the large spatial heterogeneity in
 166 topographic gradients. The distribution of the Moderate Resolution Imaging Spectroradiometer (MODIS)
 167 normalized difference vegetation index (NDVI) has a median value of ~0.6 and a maximum value
 168 approaching 1. According to the MODIS International Geosphere–Biosphere Programme (IGBP) land
 169 cover data, evergreen needleleaf forest is the most dominant vegetation cover in our model domain
 170 (Supplemental Fig. 1).

171



172

173 **Fig. 1|** WRF-Hydro model domain, topography, soil moisture observational sites, USGS stream gages,
 174 and statistics of the environmental setting. (a) The model domain covers several mountains in the Coast
 175 Ranges of central California (black box). Topography is from the USGS National Elevation Dataset
 176 (NED) 30-m DEM (shading). There are seven in-situ soil moisture stations (blue circles for NOAA PSL
 177 stations and blue triangles for WRCC stations) and nine USGS stream gages that measure natural flows

178 (purple crosses). The location of the study area in the U.S. is shown in the embedded map with the state
179 of California shaded in grey. Distributions of (b) topographic elevation, (c) topographic slope, and (d)
180 normalized difference vegetation index (NDVI) within the model domain. Median values of the
181 distributions are indicated by the black vertical dashed lines and 25th and 75th percentiles are indicated by
182 the orange vertical dashed lines. The distributions of elevation and slope are calculated using the USGS
183 30-m DEM, and the distribution of NDVI is calculated based on the Aqua Moderate Resolution Imaging
184 Spectroradiometer (MODIS) Vegetation Indices (MYD13Q1) Version 6.1 data.

185

186

187 **3. Data and Methods**

188 **3.1 WRF-Hydro model description and configurations**

189 WRF-Hydro is a physics-based, open-source community model that simulates 3-D land surface
190 hydrologic processes (Gochis et al. 2020). WRF-Hydro includes the Noah-MP Land Surface Model (LSM)
191 (Niu et al. 2011), a terrain routing module, a channel and reservoir routing module, and a conceptual
192 baseflow bucket model. The Noah-MP LSM simulates vertical energy fluxes (i.e., sensible and latent heat
193 and net radiation), moisture fluxes (i.e., infiltration, infiltration excess, canopy interception, and
194 evapotranspiration), and soil thermal and moisture state variables. In default configuration, the soil
195 column in Noah-MP LSM has a total depth of 2 m and four soil layers. The thickness of the layers from
196 top to bottom is 10, 30, 60, and 100 cm, respectively. For each of the four soil layers, the simulation of
197 water movement follows the diffusive form of Richard's equation. Users can modify the total depth and
198 thickness of each layer but in the current version of WRF-Hydro the total soil depth and vertical
199 distribution of soil layers can only be the same across the model domain.

200 Soil moisture and other variables are disaggregated from the relatively coarse grid in Noah-MP LSM
201 (1-km in our study) to the higher resolution grid in the terrain routing module (100-m in our study) which
202 then simulates subsurface and overland flow. The high-resolution terrain routing grid is generated by
203 interpolating the USGS NED 30-m hydrologically-conditioned DEM to our 100-m grid. Once the
204 overland flow and subsurface flow simulated from the terrain routing module flow into the channel grid
205 that is pre-defined in the USGS hydrologically-conditioned DEM, the channel routing module of WRF-
206 Hydro routes the water as channelized streamflow. The channel routing module works at a spatial
207 resolution consistent with the channel bottom width which typically ranges from 1.5 m to 100 m. More
208 details regarding the governing equations and model workflows can be found in Li et al. (2022).

209 In this study, WRF-Hydro is run in standalone mode, i.e., it is not coupled with an atmospheric model.
210 We use the Multi-Radar/Multi-Sensor System (MRMS) gauge-corrected quantitative precipitation
211 estimation (QPE; Zhang et al., 2011, 2014, 2016) to provide precipitation forcing at hourly, 1-km
212 resolution and the Phase 2 of North American Land Data Assimilation System (NLDAS-2) to provide
213 forcing of other meteorological variables including incoming shortwave and longwave radiation, specific
214 humidity and air temperature at 2 m above the surface, surface pressure, and 10-m wind speed (both u and
215 v components) at hourly, 1/8-degree resolution. The MRMS precipitation and NLDAS-2 forcing data are
216 re-gridded onto the 1-km Noah-MP LSM grid using bilinear interpolation.

217 WRF-Hydro is initialized with National Centers for Environmental Prediction (NCEP) FNL (Final)
218 Operational Global Analysis data. We spin up the model for one year from October 1, 2015 – September
219 31, 2016. The one-year spin-up time allows the hydrological variables in the model to reach equilibrium.
220 We run WRF-Hydro in three configurations: one in its default configuration and two calibrated
221 experiments. Details of the calibration experiments are given in Section 3.3.2. Soil moisture is reported
222 hourly on the terrain routing grid (100-m) under three configurations for October 1, 2016 to May 31, 2017.

223

224 **3.2 Soil hydraulic properties in default WRF-Hydro**

225 Prior to calibration, we performed sensitivity experiments to identify highly-sensitive soil moisture-
226 relevant parameters in WRF-Hydro (Supplemental Fig. 2). Our sensitivity experiments covered numerous
227 soil property and vegetation parameters including *smcmax* (soil porosity), *dksat* (saturated hydraulic
228 conductivity), *bexp* (coefficient *b* in Cosby et al. (1984) that denotes pore size distribution), *smcref* (field
229 capacity), *smcwlt* (wilting point), *slope* (bottom soil layer drainage), *rsurfexp* (surface dryness factor
230 controlling the surface resistance for evaporation), *hvt* (canopy height), and *vcmx25* (maximum
231 carboxylation rate at 25°C). The sensitivity analyses were performed by manually changing the parameter
232 values within a physically-reasonable range based on POLARIS and comparing changes in simulated soil
233 moisture time series. Eventually *smcmax*, *dksat*, and *bexp* were identified as the three most sensitive
234 parameters and their effects on soil moisture simulations are shown in Supplemental Fig. 2.

235 In the default version of the Noah-MP LSM and WRF-Hydro, *smcmax*, *dksat*, and *bexp* are mapped
236 onto the 16 soil classes defined in the 1-km USDA State Soil Geographic database (STATSGO; Miller
237 and White, 1998) based on the soil analysis from Cosby et al. (1984) (Fig. 2a–c and Supplemental Table
238 1). Specifically, Holtan et al. (1968) and Rawls et al. (1976) collected 1448 soil samples from 35
239 locations across 23 states in the U.S. Using these soil samples, Cosby et al. (1984) derived the
240 representative values of soil saturated hydraulic conductivity and porosity for each soil class, whereas the

241 *bexp* (i.e., *b* in the equation below) was calculated via a best fit to the moisture retention data. This soil
242 analysis conducted by Cosby et al. (1984) is used as the default soil hydraulic properties in WRF-Hydro
243 (Supplemental Table 1). The 16-type STATSGO soil map has a relatively coarse spatial resolution and its
244 accuracy was found to be questionable (Dy and Fung, 2016).

245

246 **3.3 A new soil data-informed calibration method**

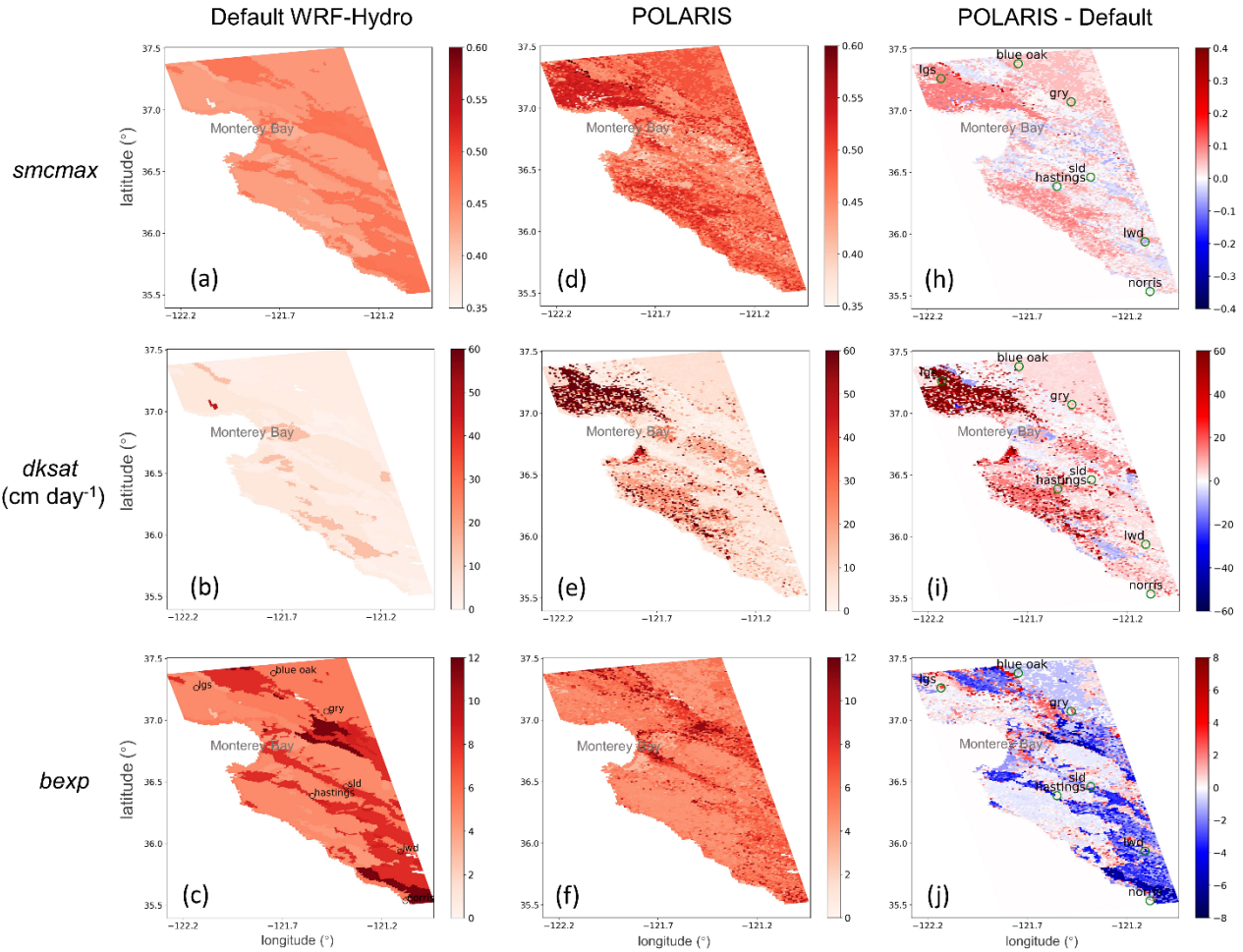
247 **3.3.1 SSURGO and POLARIS soil databases**

248 To better constrain the uncertainties in the soil parameters of WRF-Hydro, we leverage two related
249 open access soil databases, i.e., the Soil Survey Geographic (SSURGO) database and the probability
250 mapping of SSURGO (POLARIS; Chaney et al. 2016). Here we provide a brief description of both.

251 SSURGO is a compilation of soil surveys with details gathered over the course of a century for the
252 CONUS (Soil Survey Staff, 2021). It was generated via a combination of observed soil information in the
253 field, lab experiments, expert knowledge, areal images, pedotransfer functions, and extrapolation of
254 observations using soil and/or landscape models. It is managed and updated annually by the National
255 Cooperative Soil Survey. In terms of data format, SSURGO provides a map of polygon features with
256 assigned unique map units and tabular soil texture and property information. Each map unit corresponds
257 to multiple soil components and each component corresponds to multiple soil horizons. Though it has the
258 highest level of details and it is the most up-to-date soil physical property data, it is subject to data gaps
259 and artificial discontinuities between political units that conduct the soil survey (i.e., county or state
260 boundaries).

261 To fill the data gaps, remove the artificial discontinuities, and spatially disaggregate the multiple
262 components for one map unit in SSURGO, POLARIS probabilistically remaps SSURGO using high-
263 resolution geospatial environmental data such as topography and land cover data with a random forest
264 machine learning algorithm (DSMART-HPC; Chaney et al., 2016). POLARIS provides soil series
265 predictions with uncertainties for six soil layers at 30-m resolution over CONUS. The statistics it provides
266 include the mean, mode, 5th, 50th, and 95th percentiles and the depths of the six soil layers are 0–5 cm,
267 5–15 cm, 15–30 cm, 30–60 cm, 60–100 cm, and 100–200 cm, respectively.

Soil Hydraulic Properties



268

269 **Fig. 2|** Maps of soil hydraulic properties including *smcmax* (porosity), *dksat* (saturated hydraulic
270 conductivity; cm day^{-1}), and *bexp* that controls the soil pore size distribution in (a)–(c) default WRF-
271 Hydro, (d)–(f) POLARIS-based parameters, and (h)–(j) difference between the POLARIS-based
272 parameters and default WRF-Hydro. Note that (d) and (e) show the median porosity and saturated
273 hydraulic conductivity from 0–5 cm soil layer in POLARIS and *bexp* in (f) is calculated using the
274 POLARIS 0–5 cm median clay fraction based on the linear regression model in Cosby et al. (1984). The
275 green circles in (h) – (j) show the seven in-situ soil moisture stations.

276

277 3.3.2 Soil data-informed calibration experiments

278 In this study, except for the experiment using default WRF-Hydro, we perform two WRF-Hydro
279 calibration experiments by incorporating the information from SSURGO and POLARIS. Fig. 3 shows a
280 flowchart summarizing the information and methods used in the two experiments, i.e., 1) POLARIS-

281 calibrated WRF-Hydro with a 2 m soil column (hereafter referred to as “POLARIS-calibrated WRF-
282 Hydro”) and 2) the POLARIS-calibrated WRF-Hydro with a modified total soil thickness of 40 cm
283 (hereafter referred to as “POLARIS-40 cm soil”). It is worth mentioning that reducing total soil thickness
284 does not influence surface soil moisture simulations so POLARIS-40 cm soil experiment simulates the
285 same surface soil moisture as POLARIS-calibrated WRF-Hydro. We perform both calibration
286 experiments starting October 1, 2016 and both calibrated and default WRF-Hydro run for eight months
287 from October 1, 2016 – May 31, 2017.

288 In the POLARIS-calibrated WRF-Hydro, we use the median values in the top soil layer (0–5 cm) of
289 the following parameters: porosity (in $\text{m}^3 \text{ m}^{-3}$), saturated hydraulic conductivity on \log_{10} scale (cm hr^{-1}),
290 and clay fraction (in %). We use median values because they are more representative for the entire
291 distribution. Specifically, the median POLARIS porosity and saturated hydraulic conductivity are re-
292 gridded onto the Noah-MP LSM grid using a nearest-neighbor interpolation and are used to replace the
293 parameters *smacmax* and *dksat* in all four soil layers in default WRF-Hydro (Fig. 2d&e). To derive *bexp*
294 which denotes the soil pore size distribution (Fig. 2f), we re-grid the median clay fraction onto the LSM
295 grid and apply a linear regression model adopted from Cosby et al. (1984):

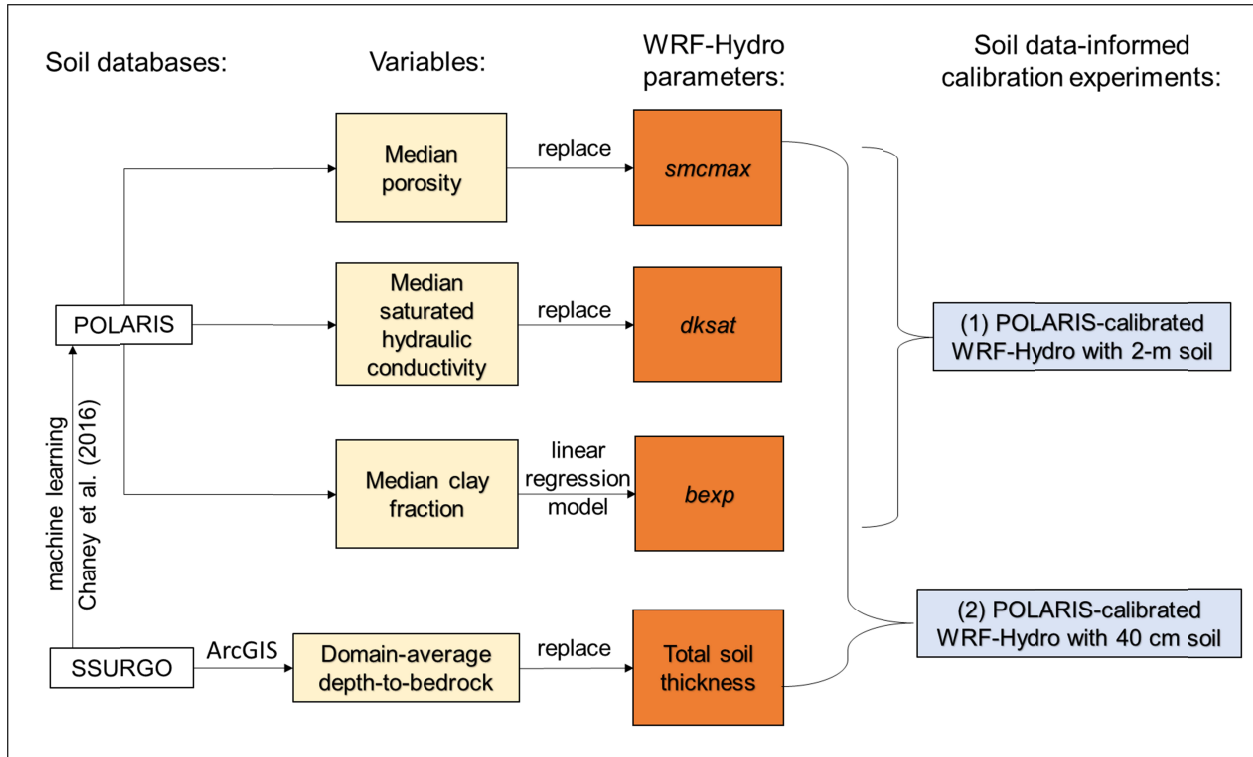
$$296 \quad bexp = 0.159 \times c + 2.91 \quad (1)$$

297 where *c* is clay fraction in %. Differences between the POLARIS-based and default soil parameters are
298 displayed in Fig. 2h,i&j.

299 In the second calibration experiment, we set up the model domain of POLARIS-calibrated WRF-
300 Hydro with a reduced total soil thickness of 40 cm, and each of the four soil layers has a thickness of 10
301 cm. 40 cm is derived via calculating the domain average of the depth-to-bedrock data from SSURGO.
302 Based on SSURGO, the soil depth in our model domain ranges from 0–173 cm with a mean and a
303 standard deviation of 40 and 39 cm, respectively (Supplemental Fig. 3). Therefore, the 2-m soil in the
304 default setting of WRF-Hydro is likely overestimating the actual soil conditions in central California.

305

306



307

308 **Fig. 3|** A schematic flowchart summarizing the datasets, variables, model parameters, and methods used
 309 in our soil data-informed calibration experiments: (1) the POLARIS-calibrated WRF-Hydro, and (2) the
 310 POLARIS-40 cm soil according to the domain average of the SSURGO depth-to-bedrock data.

311

312

313 **3.4 Model performance evaluation**

314 **3.4.1 Soil moisture in-situ stations and USGS streamflow gages**

315 We then evaluate both the default and the calibrated WRF-Hydro against soil moisture and
 316 streamflow observations over October 1, 2016 – May 30, 2017 at hourly time steps. It is noteworthy that
 317 most stream gages in our study area experience no-to-low flows outside the period of December to March.
 318 Therefore, although our model evaluations span the whole 8-month period (October 2016 – May 2017),
 319 we find a similar conclusion when evaluating the streamflow just for December to March.

320 The soil moisture observations we use in this study is volumetric soil moisture indirectly measured at
 321 seven in-situ stations. The water content reflectometers CS616 and CS625 at the four PSL stations (sld,
 322 lgs, gry, and lwd) measure the soil temperature and output period at 10 cm below ground at 2-minute
 323 interval. We use these two variables to compute the volumetric soil moisture. We firstly perform a data

324 correction to the output period with the measured soil temperature following the equation in the
325 reflectometer instruction manual (Campbell Scientific INC, retrieved 2021):

$$326 \quad \tau_c(T) = \tau_o + (20 - T) \times (0.526 - 0.052 * \tau_o + 0.00136 * \tau_o^2) \quad (2)$$

327 where τ_o and τ_c are output periods in microseconds before and after the correction, respectively, and T is
328 soil temperature in °C. The corrected output period is then converted to volumetric soil water content (m^3
329 m^{-3}) using a quadratic calibration equation documented in the instruction manual (Campbell Scientific
330 INC, retrieved 2021):

$$331 \quad VWC = -0.0663 - 0.0063 \times \tau_c + 0.0007 \times \tau_c^2 \quad (3)$$

332 At the three WRCC stations (blueoak, hastings, and norris), reflectometer CS615 is used to measure
333 the soil moisture at 2 inches (~5 cm) below ground at 10-minute resolution.

334 To compare WRF-Hydro soil moisture simulations with the in-situ observations, we first compute the
335 hourly mean for the soil moisture observations during October 1, 2016 – May 31, 2017. Next, time series
336 of soil moisture simulations are collected from the WRF-Hydro high-resolution routing grid cells (100-m)
337 that are closest to the seven observational stations. We also use the in-situ precipitation recorded by the
338 soil moisture observational stations to investigate the uncertainties in the precipitation forcing (i.e., the
339 MRMS).

340 Nine USGS stream gages with natural flows (i.e., no human regulation) are available in our model
341 domain, as shown in Figure 1a. They are Saratoga Creek at Saratoga (ID 11169500), Soquel Creek at
342 Soquel (ID 11160000), WB Soquel C NR Soquel (ID 11159800), Corralitos Creek at Freedom (ID
343 11159200), Tres Pinos Creek near Tres Pinos (ID 11157500), Arroyo Seco NR Soledad (ID 11152000),
344 Arroyo Seco BL Reliz C NR Soledad, CA (ID 11152050), San Antonio River near Lockwood (ID
345 11149900), and Nacimiento River below Sapaque Creek near Bryson (ID 11149800). The streamflow
346 observations are at 15-minute resolution and we calculate the hourly mean of the observations to compare
347 with our model simulations.

348

349 **3.4.2 Other remotely-sensed and LSM-simulated soil moisture products**

350 For further evaluation of the performance of WRF-Hydro simulated soil moisture, we also compare
351 POLARIS-calibrated soil moisture with four other widely-used soil moisture products: SMAP L4,
352 NLDAS-2 Noah, VIC, and Mosaic LSMs.

353 SMAP L4 is a merged soil moisture product that assimilates SMAP satellite L-band brightness
354 temperature observations into the NASA's GEOS-5 Catchment LSM using a spatially-explicit ensemble
355 Kalman filter (Reichle et al., 2017). Catchment LSM has a temporal resolution of 3 hours, a spatial
356 resolution of 9 km, and provides soil moisture estimates at the surface (0–5 cm) and root zone (0–1 m).
357 SMAP L4 is chosen because SMAP satellite-derived soil moisture has been reported to be superior to
358 other remotely-sensed soil moisture products by various studies (Al-Yaari et al., 2017; Zhang et al., 2017;
359 Chen et al., 2018; Kumar et al., 2018; Tavakol & Rahmani, 2018) (Ford and Quiring 2019). Compared to
360 SMAP L1–3 products, SMAP L4 is continuous over space and time and combines both observation and
361 simulation components.

362 NLDAS-2 applies state-of-the-art observational and simulated data as forcing to drive physically-
363 based, uncoupled, distributed LSMs to simulate land surface conditions at hourly and 1/8-degree
364 resolutions over the U.S. NLDAS-2 uses three physics-based LSMs, i.e., Noah (Betts et al., 1997; Chen et
365 al., 1997), VIC (Liang et al., 1994), and Mosaic (Koster and Suarez, 1994, 1996). All NLDAS-2 LSMs
366 share the same atmospheric forcing, soil classification, and land cover, but they yield different results due
367 to different model physics, configuration, and parameter choices. Noah-LSM was developed as the land
368 component of the mesoscale Eta model by NOAA and NCEP (Betts et al., 1997; Chen et al., 1997). It
369 also works as the LSM of WRF atmospheric model and NOAA/NCEP Global Forecast System (GFS) and
370 Climate Forecast System (CFS). Noah has four soil layers with depths of 10, 30, 60, and 100 cm from top
371 to bottom. VIC-LSM is a macroscale, semi-distributed hydrologic model designed by University of
372 Washington and Princeton University (Liang et al., 1994; Wood et al., 1997). It has three soil layers with
373 spatially-varying layer depths depending on the vegetation type and root distribution. The Mosaic LSM
374 was developed for use in NASA's global climate models by Koster and Suarez (1994 and 1996). It uses a
375 tile approach to represent vegetation variability at sub-grid scales. Each vegetation tile simulates its own
376 soil moisture and consists of three soil layers with depths of 10, 30, and 160 cm from top to bottom. The
377 soil moisture from NLDAS-2 LSMs has been widely evaluated (Xia et al. 2015; Xia et al. 2014; Zhuo et
378 al. 2015). In a nation-wide soil moisture product evaluation study, soil moisture simulations from
379 NLDAS-2 LSMs are found to have the best performance among various modeled and remotely sensed
380 soil moisture products (Ford and Quiring 2019).

381 We average soil moisture observations and WRF-Hydro simulations to 3-hourly to compare with the
382 surface-layer, 3-hourly SMAP L4 soil moisture. For the three NLDAS-2 LSMs, we use the hourly soil
383 moisture product in the surface layer. We perform both point-scale and spatial comparisons between
384 calibrated WRF-Hydro and the four soil moisture products. For comparisons at observational site level,
385 soil moisture simulated at the LSM grid points that are closest to the seven in-situ stations are evaluated

386 against the seven observational stations and the evaluation metrics are compared with those in the
387 calibrated WRF-Hydro (Section 4.3). For spatial comparisons, soil moisture in WRF-Hydro is
388 interpolated to the grids of the Catchment, Noah, VIC, and Mosaic LSMs using bilinear interpolation, and
389 the evaluation metrics are calculated for each products' time series at each grid (Supplemental Text 2).

390

391 **3.4.3 Evaluation metrics**

392 To evaluate model performance, we use five metrics including the Pearson correlation coefficient (r),
393 mean bias, root mean square error (RMSE), mean absolute error (MAE), Kling-Gupta Efficiency (KGE)
394 (Gupta et al. 2009; Kling et al. 2012), and Nash-Sutcliffe Efficiency (NSE) (Nash and Sutcliffe 1970).

395 KGE is a comprehensive metric used to evaluate the performance of hydrologic models, and has been
396 applied in other studies to evaluate soil moisture simulations (Lahmers et al. 2019; Vergopolan et al.
397 2020). It is calculated as follows:

398
$$KGE = 1 - \sqrt{(r - 1)^2 + (\alpha - 1)^2 + (\beta - 1)^2}, \quad (4)$$

399 where r is the correlation coefficient between the simulation and observation, α is the ratio of the
400 standard deviation of simulation to that of the observation, and β is the ratio of the mean of simulation
401 to that of the observation. A model has higher fidelity to observations if KGE and r are closer to 1 and if
402 MAE and RMSE approach 0.

403 NSE is commonly used to evaluate the performance of streamflow simulations in hydrologic models
404 (Wang et al. 2019; Xia et al. 2012). It is calculated as follows:

405
$$NSE = 1 - \frac{\sum_{t=1}^{t=T} (Q_{sim}(t) - Q_{obs}(t))^2}{\sum_{t=1}^{t=T} (Q_{obs}(t) - \bar{Q}_{obs})^2}, \quad (5)$$

407 where T is the length of the time series, $Q_{obs}(t)$ and $Q_{sim}(t)$ are observed and simulated discharge at
408 time t , respectively, and \bar{Q}_{obs} denotes the mean observed discharge over time. Generally, NSEs of 1
409 stand for a perfect model-observation match and NSE values approaching 1 indicate excellent model
410 performance in simulating streamflow. Typically, NSEs that are between 0.5 and 0.65 are suggested to
411 be an indication of sufficient model performance (Wang et al. 2019) and negative NSEs represent poor
412 model performance (Schaeefli and Gupta 2007).

413 **4. Results**

414 **4.1 Simulations of soil moisture with POLARIS-calibrated WRF-Hydro**

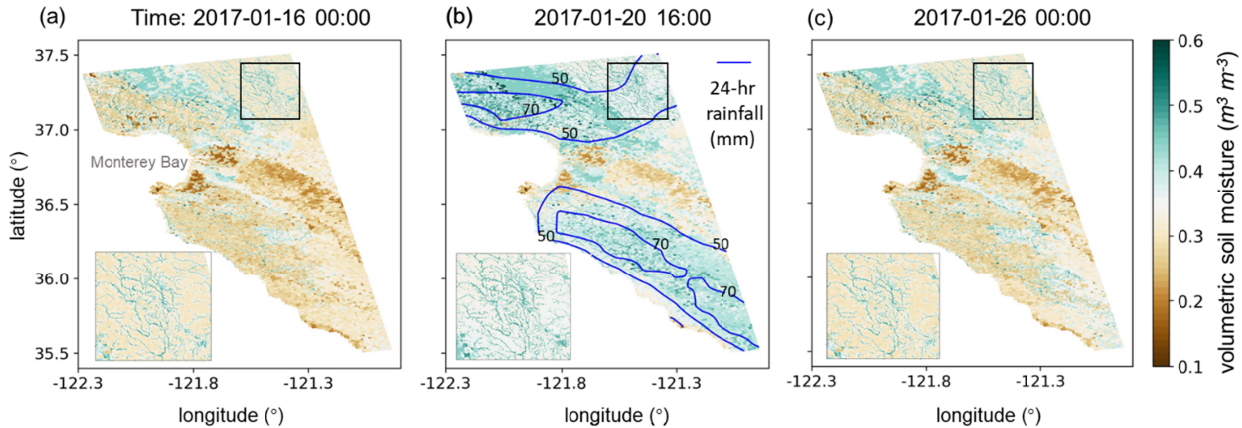
415 In this study, we use the fully-distributed WRF-Hydro to simulate soil moisture at high spatial (100-m)
416 and temporal (hourly) resolutions in a central California domain and we leverage observation-based soil
417 databases to inform model calibration (see details regarding the POLARIS dataset and calibration method
418 in Section 3.3). In POLARIS-calibrated WRF-Hydro, default parameters are replaced with POLARIS-
419 based soil parameters. Differences are evident between the POLARIS-based and default soil parameters
420 (Fig. 2h–j). We find that the 16 soil parameters in the default version of WRF-Hydro underestimate the
421 spatial heterogeneity of soil characteristics in the field, while the more spatially refined POLARIS-based
422 soil parameters display greater spatial variation (Fig. 2).

423 To visualize the simulation of soil moisture in WRF-Hydro over space and time, Fig. 4 shows the
424 simulated evolution of surface soil moisture before, during, and after a storm event in the POLARIS-
425 calibrated WRF-Hydro. The three time slices shown in Fig. 4 are marked by vertical dashed lines in Fig.
426 5a. The chosen storm spanned 5 days from January 16, 2017 to January 20, 2017 with a maximum
427 precipitation intensity of $\sim 240 \text{ mm day}^{-1}$ according to MRMS. During this storm event, the soil moisture
428 at many stations reached their maximum value over our study period. WRF-Hydro simulates the wetting
429 and drainage processes related to the passing of the storm. The high-resolution terrain routing module of
430 WRF-Hydro is able to simulate the interactions between hydrology and the microtopography at finer
431 scales. In addition, the channel routing module of WRF-Hydro simulates channelized streamflow at scales
432 comparable to the channel widths ranging from 1.5 to 100 m, such that WRF-Hydro can simulate greater
433 level of details including the elevated surface soil moisture within channel networks (zoomed-in maps in
434 Fig. 4).

435

436

WRF-Hydro simulated surface soil moisture during a storm



437

438 **Fig. 4|** Evolution of surface soil moisture simulated by the POLARIS-calibrated WRF-Hydro (a) before a
439 storm (2017 January 16 00:00), (b) during the soil moisture peak (2017 January 20 16:00), and (c) after a
440 storm event (2017 January 26 00:00). The three time slices are marked by vertical dashed lines (i), (ii),
441 and (iii) in Fig. 5a, respectively. Embedded maps in the bottom left show zoomed-in details of soil
442 moisture in and near channel networks within the black boxes. 24-hr accumulated precipitation (mm; blue
443 contours) from 00:00 to 23:59 on January 20, 2017 is shown in (b) and contours of 50, and 70 mm are
444 labeled. 24-hr accumulated precipitation for January 16 and 26, 2017 have zeros everywhere.

445

446 **4.2 Evaluation of WRF-Hydro soil moisture against in-situ soil moisture**

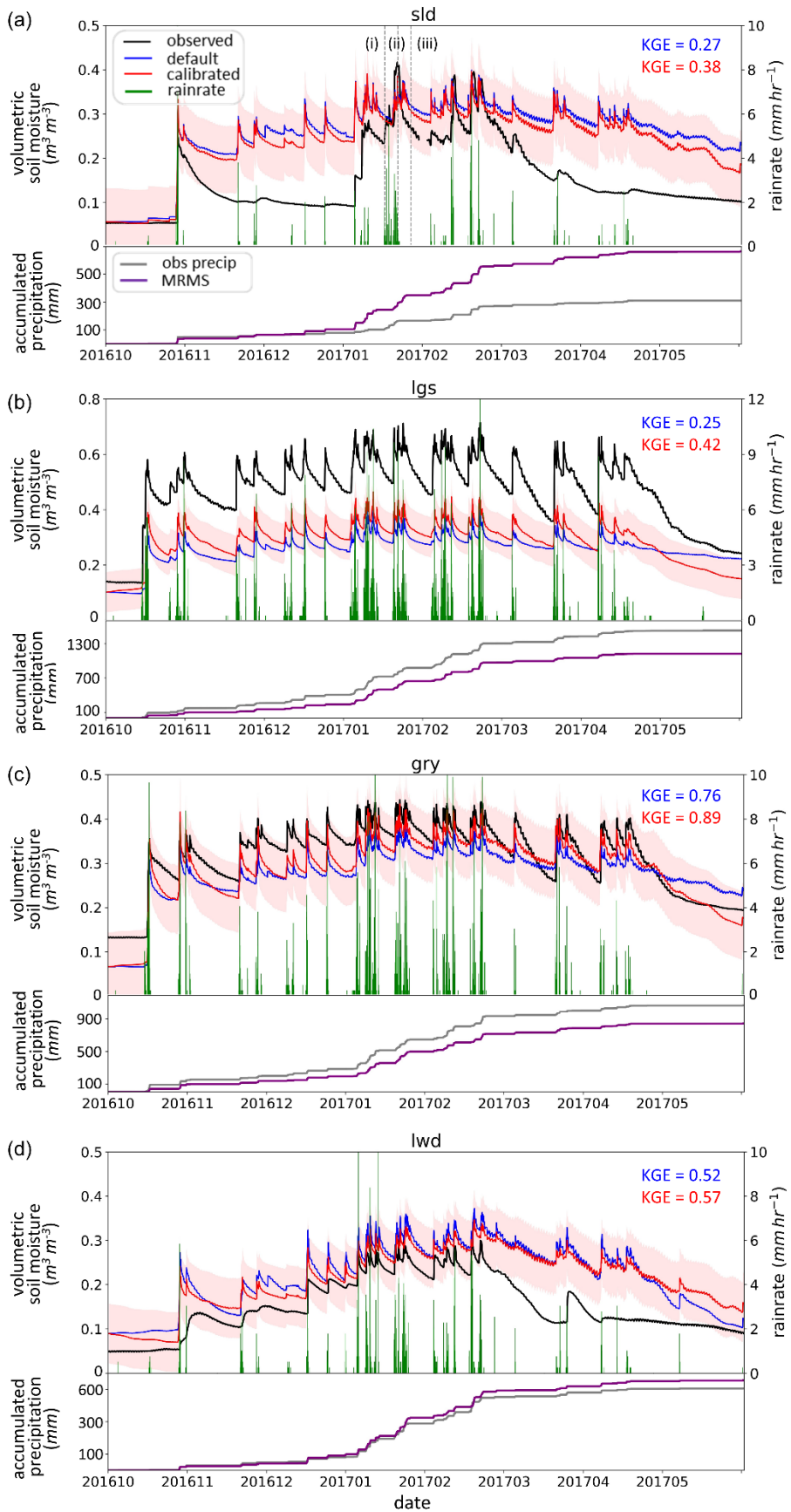
447 To assess the performance of our POLARIS-calibrated WRF-Hydro, soil moisture time series before
448 and after calibration are compared with the observations at seven in-situ stations (Figs. 5&6). Generally,
449 both default and POLARIS-calibrated WRF-Hydro capture the magnitude and variability of the
450 observations, and the ± 1 standard deviation simulation envelope for POLARIS-calibrated WRF-Hydro
451 encapsulates the observed soil moisture during the majority of the study period for most stations (Figs.
452 5&6). After the POLARIS-informed calibration, r increases at six of the seven stations, while RMSE and
453 MAE decrease and KGE increases across all in-situ stations (Supplemental Table 2). The average
454 correlation coefficient across the seven stations increases from 0.84 to 0.89, mean RMSE decreases from
455 $0.0916 \text{ m}^3 \text{ m}^{-3}$ to $0.0754 \text{ m}^3 \text{ m}^{-3}$, and mean KGE increases from 0.57 to 0.67. Four of seven stations have
456 above-average KGEs. Stations gry, hastings, and norris have KGE values above 0.85. Compared to the
457 default WRF-Hydro simulation, the average of the percent change in correlation coefficients across seven
458 stations increases by ~6%, the average RMSE percent change decreases ~18%, and average KGEs

459 increase ~25%, indicating skill improvements in POLARIS-calibrated WRF-Hydro to simulate surface
460 soil moisture.

461 Our results show that the POLARIS-calibrated WRF-Hydro performs reasonably well during the wet
462 season (October 2016 – February 2017 in our case). Mean KGE during the wet season across seven
463 stations reaches 0.74. However, its performance over the entire study period is negatively affected by the
464 performance during the dry season (starting March 2017 in our case). Dry-season mean KGE across seven
465 stations drops to 0.45. Model performance varies the greatest between wet and dry periods at stations sld,
466 lwd, and norris. KGE values for stations sld, lwd, and norris during 2016 October 1 – 2017 February 28
467 (wet season) are 0.52, 0.77, and 0.97, respectively, and 0.13, 0.09, and 0.52 during 2017 March 1 – May
468 31 (dry season). In these stations, moisture in the surface soil layer decreases more slowly during dry
469 weather conditions than observations indicate (Fig. 5a&d & Fig. 6c). Based on the sensitivity experiments
470 we performed prior to our calibration, both *smcmax* and *bexp* can greatly impact the dry-period water
471 drainage rate (from April 15 onwards in Supplemental Fig. 2). Accordingly, we hypothesize that wet
472 biases simulated during the dry period are related to the uncertainties of these two parameters.

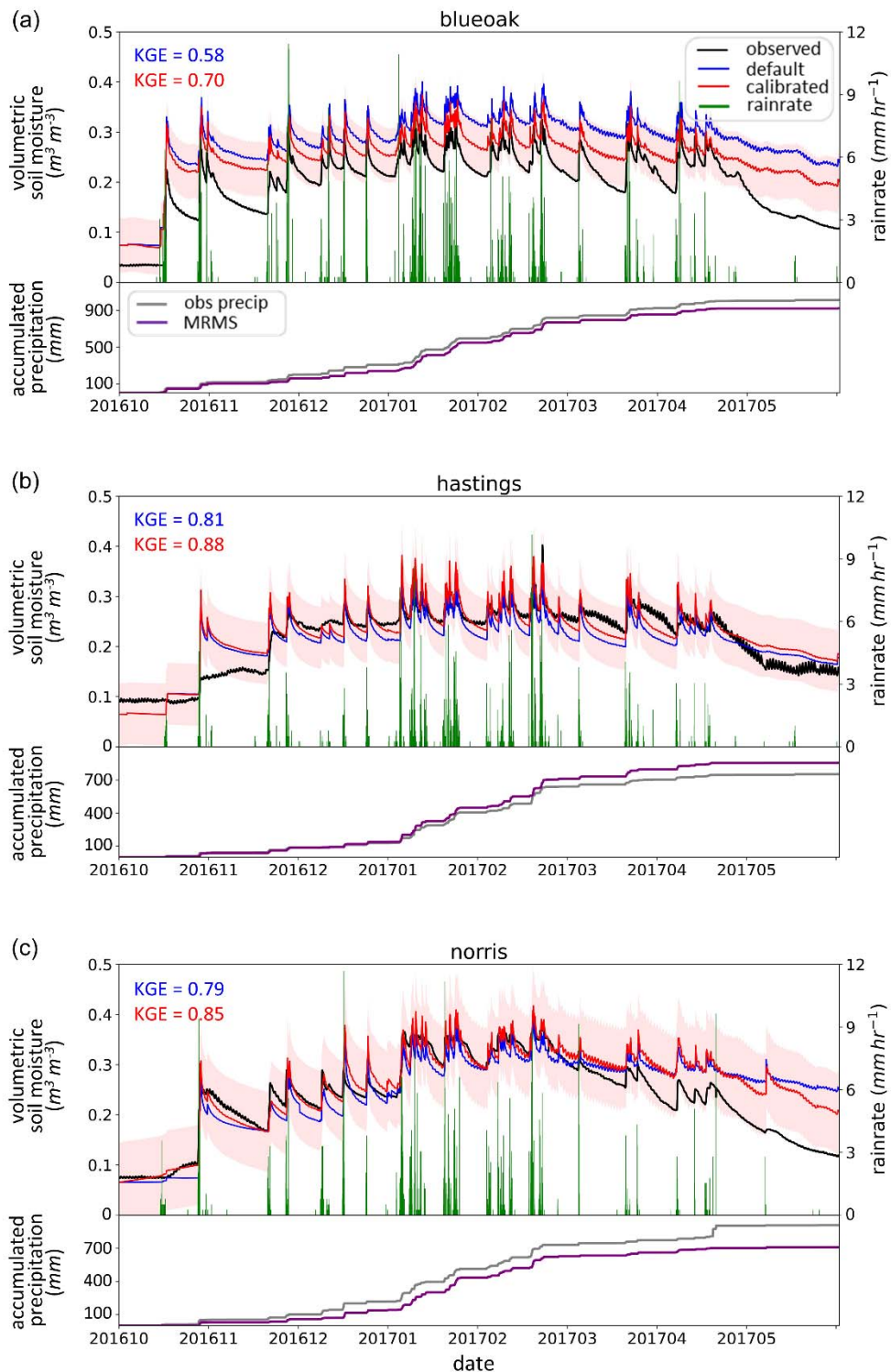
473 In addition to uncertainties in model parameters, another important source of uncertainty that leads to
474 differences between the observations and simulations, especially during the wet season, is the
475 uncertainties of MRMS precipitation. By comparing MRMS precipitation with observational precipitation
476 measured at the seven sites, we found that model biases at stations sld and lgs, which are the two stations
477 with the lowest KGE scores, can be largely explained by the discrepancies in precipitation (Fig. 5a&b;
478 Supplemental Table 2). At station sld, the accumulated precipitation total during the 8-month study period
479 is more than double of that found in MRMS, whereas at station lgs the in-situ precipitation is ~35%
480 higher than the MRMS, leading to the positive bias at sld and negative bias at lgs (Fig. 5a&b). For station
481 gry, MRMS precipitation underestimates the in-situ precipitation by ~25%, which also agrees with the
482 negative mean bias in our WRF-Hydro simulations (Fig. 5c; Supplemental Table 2). The discrepancy in
483 accumulated precipitation amount at station norris is consistent with the dry bias in modeled soil moisture
484 before March 2017 (Fig. 6c). During March – May 2017, however, the parameter uncertainties associated
485 with *smcmax* and *bexp* are likely causing the positive model bias (Supplemental Fig. 2). The differences
486 in accumulated precipitation at the other three sites are relatively small (Figs. 5d & 6a&b).

487



489 **Fig. 5|** Volumetric soil moisture time series and accumulated precipitation amount from 2016 October 1
490 to 2017 May 31 at NOAA PSL in-situ soil moisture stations (a) sld, (b) lgs, (c) gry, and (d) lwd. Top
491 panels in (a)–(d) show volumetric soil moisture in the observations (in $\text{m}^3 \text{ m}^{-3}$; black line), default WRF-
492 Hydro simulation (in $\text{m}^3 \text{ m}^{-3}$; purple line), and POLARIS-calibrated WRF-Hydro simulation (in $\text{m}^3 \text{ m}^{-3}$; red line). The pink color shading shows the ± 1 standard deviations around the POLARIS-calibrated
493 simulation. Hourly precipitation rate in MRMS is shown in green bars (mm hr^{-1}). Grey vertical dashed
494 lines marked with (i), (ii), and (iii) in (a) indicate the three time slices shown in Fig. 4a-c, respectively.
495 Bottom panels in (a)–(d) show the accumulated precipitation measured at the in-situ soil moisture stations
496 (in mm; grey line) and in the MRMS gauge-corrected quantitative precipitation estimation (QPE; in mm;
497 purple line). The accumulated MRMS precipitation is calculated by summing up the precipitation falling
498 on the grid points that are closest to the stations. KGE values are shown in the top right for default
499 simulations (blue) and POLARIS-calibrated simulations (red).

501



502

503 **Fig. 6|** As in Fig. 5 but for the WRCC soil moisture stations (a) blueoak, (b) hastings, and (c) norris. KGE
 504 values are shown in the top left for default (blue) and POLARIS-calibrated simulations (red).

505

506

507 **4.3 Comparisons of POLARIS-calibrated WRF-Hydro with other soil moisture products**

508 Next, we compare four other soil moisture products (i.e., SMAP L4, NLDAS-2 Noah, VIC, and
509 Mosaic LSMs) against POLARIS-calibrated WRF-Hydro at the seven in-situ soil moisture observing
510 stations. In general, all five soil moisture products capture the broad variabilities in the observations at
511 sub-daily to sub-seasonal scales (Supplemental Fig. 4). Stations lgs, gry, and blueoak have relatively
512 smaller inter-model variations, whereas the inter-model difference is the largest at stations lwd, hastings,
513 and norris (Supplemental Fig. 4). For stations hastings and norris, the inter-model range roughly
514 encapsulates the observation, whereas at other stations, there are systematic positive or negative biases in
515 all products throughout the study period.

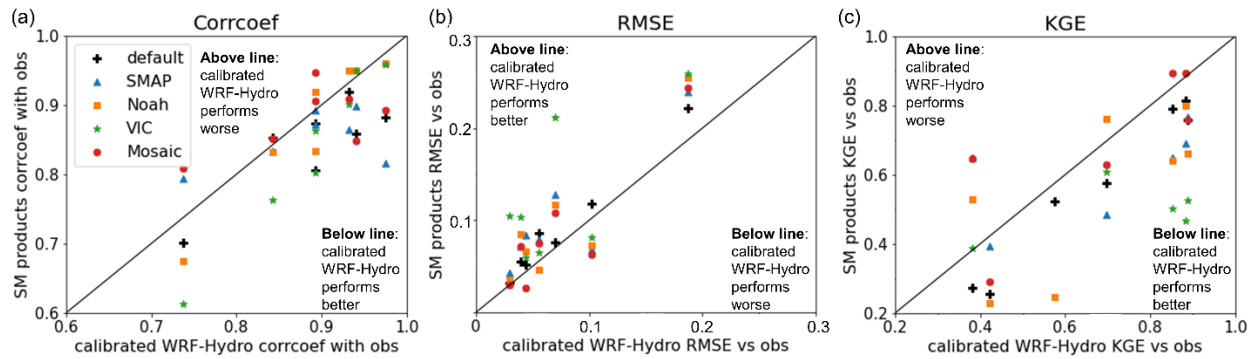
516 On average, we find that POLARIS-calibrated WRF-Hydro has the best performance in that it has the
517 highest mean KGE across seven stations ($\overline{KGE}=0.67$). Mean KGEs for SMAP L4, Noah, VIC, and
518 Mosaic LSMs are 0.53, 0.55, 0.31, and 0.61, respectively. The KGE scores are the highest in POLARIS-
519 calibrated WRF-Hydro at three of seven stations (i.e., lgs, gry, and lwd) and the second highest at stations
520 blueoak, hastings, and norris. At station sld, POLARIS-calibrated WRF-Hydro has the lowest KGE,
521 which however, are likely explained by the uncertainties in MRMS precipitation at this station (Fig. 5a
522 and Section 4.2). KGE scores are highest in Mosaic LSM at stations hastings and norris, in SMAP L4 at
523 station sld, and in Noah LSM at station blueoak. In VIC LSM, there is a substantial wet bias at stations
524 lwd and hastings and dry bias at gry and norris (Supplemental Fig. 4 and Supplemental Table 3). Indeed,
525 the RMSE in VIC exceeds $0.2 \text{ m}^3 \text{ m}^{-3}$ at stations lgs and lwd and is over $0.1 \text{ m}^3 \text{ m}^{-3}$ at stations gry and
526 hastings, and the KGE score in VIC is the lowest at five of seven stations among the four soil moisture
527 products and POLARIS-calibrated WRF-Hydro (Supplemental Table 3). In addition, because of the
528 limitation of L-band frequency that the radar and radiometer on SMAP spacecraft use to measure soil
529 moisture, SMAP L4 soil moisture may be biased in highly vegetated and topographically complex regions
530 like California (Supplemental Text 1).

531 We summarize our soil moisture product temporal comparison in Supplemental Tables 2&3 and in
532 scatter plot format (Fig. 7). In Fig. 7, evaluation metrics including r , RMSE, and KGE of default WRF-
533 Hydro, SMAP L4, Noah, VIC, and Mosaic LSMs are plotted against the evaluation metrics of POLARIS-
534 calibrated WRF-Hydro. Each point represents an evaluation metric of a soil moisture product at a soil
535 moisture station and how it compares with the metric of the POLARIS-calibrated WRF-Hydro at the
536 same station. In figures of r and KGE, points below the one-to-one line indicate higher performance in the

537 POLARIS-calibrated WRF-Hydro (Fig. 7a&c), whereas points above the one-to-one line in the figure of
 538 RMSEs represent reduced bias in the POLARIS-calibrated WRF-Hydro. In most cases, the POLARIS-
 539 calibrated WRF-Hydro has increased r (25 of 35 points), reduced errors (28 of 35 points), and increased
 540 KGEs (29 of 35 points), indicating its higher soil moisture fidelity compared to other soil moisture
 541 products and default WRF-Hydro (Fig. 7). The POLARIS-calibrated WRF-Hydro has either the highest
 542 or the second highest KGE at stations other than sld (Supplemental Table 3). The lowest KGE at station
 543 sld in POLARIS-calibrated WRF-Hydro can largely be explained by the large uncertainties of MRMS
 544 precipitation as we show in Fig. 5a and discussed in Section 4.2. To fully evaluate the performance of
 545 POLARIS-calibrated WRF-Hydro over our model domain, we also provide a spatial comparison between
 546 the soil moisture products in Supplemental Figs. 5–8 and a description on the comparison between
 547 POLARIS-calibrated WRF-Hydro and NLDAS-2 Mosaic LSM can be found in Supplemental Text 2.

 548
 549

r , RMSEs, KGEs of soil moisture products vs POLARIS-calibrated WRF-Hydro



550
 551 **Fig. 7|** Evaluation metrics of default WRF-Hydro and four soil moisture products (i.e., SMAP L4,
 552 NLDAS-2 Noah, VIC, and Mosaic LSMs) compared with the evaluation metrics of POLARIS-calibrated
 553 WRF-Hydro against in-situ observations. (a) Correlation coefficients, (b) RMSEs ($\text{m}^3 \text{m}^{-3}$), and (c) KGEs
 554 of default WRF-Hydro (black crosses) and other soil moisture products (SMAP L4: blue triangles, Noah:
 555 orange squares, VIC: green stars, Mosaic: red circles) versus that of POLARIS-calibrated WRF-Hydro.
 556 One-to-one line is indicated by the black solid line.

 557
 558

559 **4.4 Improved streamflow fidelity in the soil data-informed calibrated simulations**

560 Given the key role soil moisture plays in overland flow and subsurface flow production processes,
561 improved soil moisture simulation has been found to improve streamflow simulations spontaneously
562 (Aubert et al. 2003; Lee et al. 2011). In this section, we evaluate the streamflow simulations in the
563 POLARIS-calibrated WRF-Hydro to investigate the linkages between improved surface soil moisture
564 simulations and streamflow simulations in WRF-Hydro. We show that improved surface soil moisture
565 accuracy only moderately improves streamflow simulation. However, when we account for SSURGO
566 depth-to-bedrock data total soil thickness (i.e., the POLARIS-40 cm soil experiment), the effects of soil
567 moisture on streamflow fidelity are enhanced. Meanwhile, the soil moisture model fidelity in POLARIS-
568 40 cm soil experiment is not diminished.

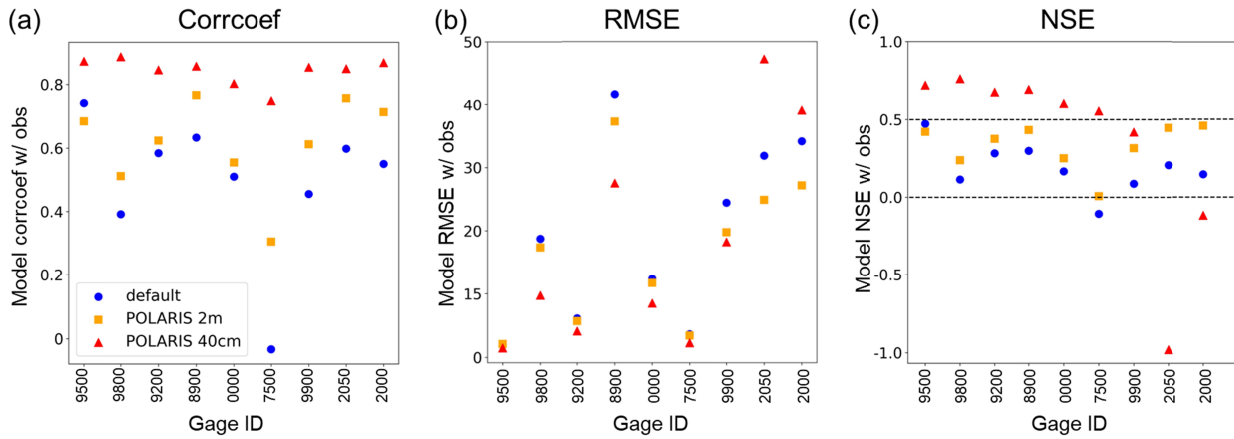
569 We show that compared to default WRF-Hydro, streamflow fidelity improves in both calibrated
570 experiments with the greatest improvement in the POLARIS-40 cm soil experiment (Fig. 8 and
571 Supplemental Table 4). In the POLARIS-calibrated WRF-Hydro with 2 m soil experiment, r increases,
572 error decreases, and NSE increases across most stations (8/9 stations see an improvement). However, the
573 improvement is quite moderate – none of the stations have NSEs above 0.5 after the calibration (Fig. 8c),
574 which suggests that improving surface soil moisture solely is not sufficient to significantly improve
575 streamflow simulation in WRF-Hydro and the total soil column needs to be considered. Indeed, model
576 performance improves by a large fraction in the POLARIS-40 cm soil experiment (Fig. 8). In the
577 POLARIS-40 cm soil experiment, r increases across all nine gages with a mean of 0.84 (p
578 value<<0.0001). Six gages have NSEs exceeding 0.5, indicating sufficient-to-good model performance in
579 these basins (Fig. 8c). RMSE decreases and NSE increases significantly at seven of the nine stations and
580 the mean NSE score across the seven improved gages reaches 0.63. At the other two gages 11152050 and
581 11152000 (Fig. 1a), however, r increases but NSE decreases to negative values in POLARIS-40 cm soil
582 experiment because the model overestimates the discharge magnitude (Fig. 8). We hypothesize that the
583 positive model bias at these two gages can be partially attributed to the overestimation in the MRMS
584 precipitation in that area. Though in-situ precipitation data is not available at USGS stream gages, we
585 make this assumption based on the fact that the two gages are located in proximity to the soil moisture
586 station sld (Fig. 1a) that has in-situ precipitation measurements. We have discussed in Section 4.2 that the
587 surface soil moisture at sld is overestimated in the POLARIS-calibrated WRF-Hydro due to the positive
588 bias in the MRMS precipitation so it is likely that streamflow simulations in POLARIS-40 cm soil
589 experiemnt are also biased high at gages 11152050 and 11152000 due to overestimated precipitation.

590 To closely examine the improvement and remaining biases after calibration, we compare the modeled
591 and observed hydrographs at three selected stations in Fig. 9. Corresponding results for the rest of the

592 stations are shown in Supplemental Figs. 9&10. The three representative gages we choose to show here
 593 are Gage 11169800 which has the highest NSE among nine stations after calibration (Fig. 9a&b), Gage
 594 11157500 which has the largest improvement in the POLARIS-40 cm soil experiment (Fig. 9c&d), and
 595 Gage 11152000 which has a diverging change in the two calibration experiments (i.e., an increased
 596 performance in POLARIS-2 m soil experiment but decreased performance in POLARIS-40 cm soil
 597 experiment) (Fig. 9e&f). Generally, POLARIS-40 cm performs the best at capturing the magnitude and
 598 timing of peak flow events among the three sets of simulations (Fig. 9). It is likely because the default 2-
 599 m soil column overestimates the realistic soil thickness in Coast Ranges of central California. With
 600 thinner soils, less water can be stored in the soil column and the hydrologic response is much faster.
 601 Indeed, in default and POLARIS-2 m soil experiments, the model underestimates the discharge
 602 magnitude especially for the storm events prior to January 15, 2017, while the POLARIS-40 cm
 603 experiment is able to capture the first few storms in January for all nine gages (Fig. 9a, c&e and
 604 Supplemental Figs. 9&10). In addition, the default WRF-Hydro does not capture any streamflow at gage
 605 11157500 during the entire time period (blue line in Fig. 9c), whereas in the POLARIS-40 cm case
 606 streamflow is simulated with a small mean bias of $-0.3 \text{ m}^3 \text{ s}^{-1}$ and an NSE of 0.56.

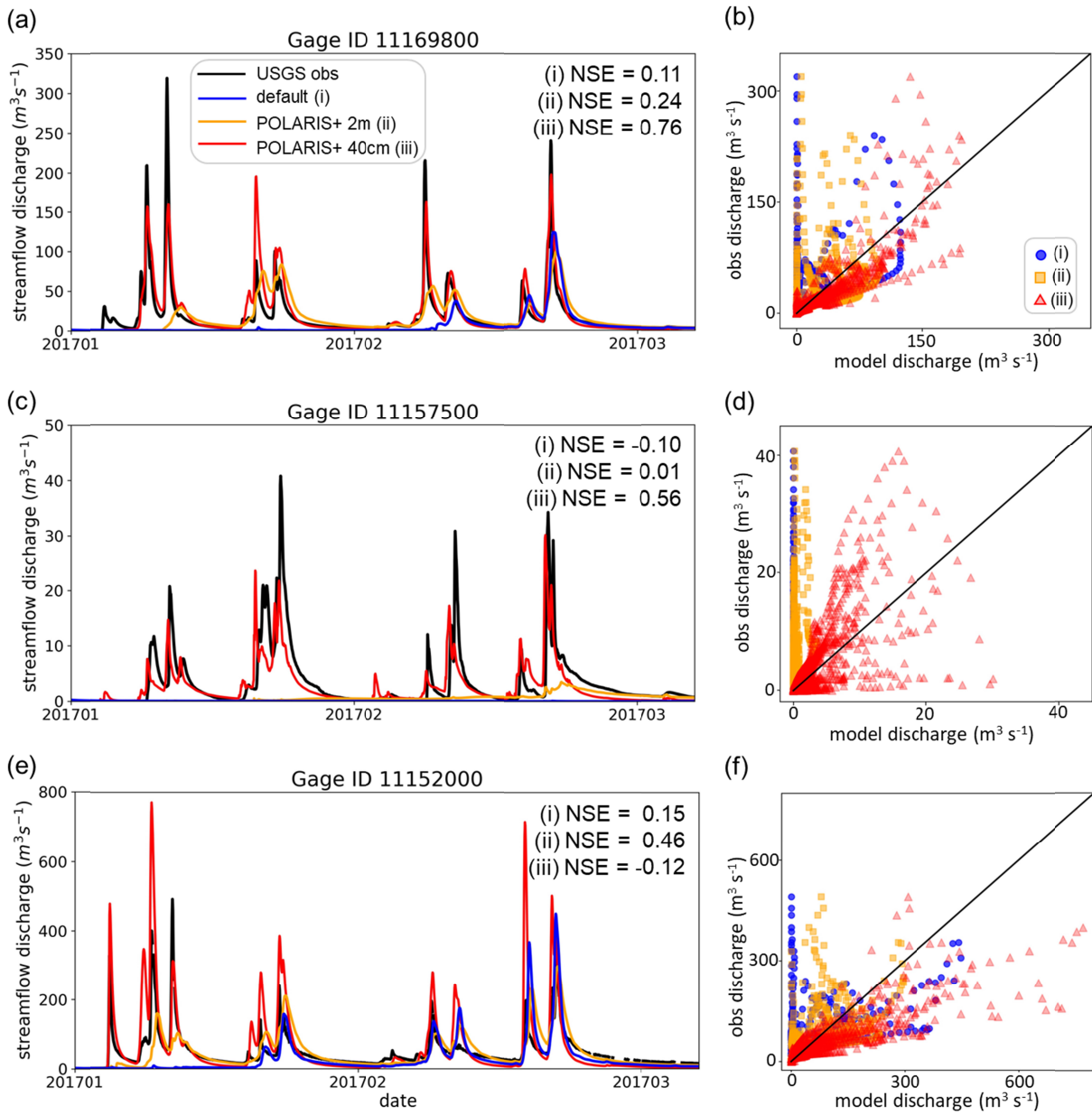
607

r, RMSEs, NSEs of streamflow in default and POLARIS-calibrated simulations



608

609 **Fig. 8|** Scatter plots of performance metrics including (a) correlation coefficients, (b) RMSEs, and (c)
 610 NSEs in the default (blue circles), POLARIS-calibrated WRF-Hydro (orange squares), and POLARIS-
 611 calibrated WRF-Hydro with 40 cm soil (red triangles). The labels on the x axes show the last 4 digits of
 612 the USGS stream gage IDs. The horizontal dashed lines in (c) indicate NSE of 0.5 and 0.0, respectively.
 613 NSE of 0.5 is suggested to be the threshold of sufficient model performance whereas NSE below 0
 614 indicates poor model performance.



617 **Fig. 9|** (a), (c), and (e) Streamflow hydrographs of USGS stream observations (black line), default WRF-
618 Hydro (blue line; labeled with (i)), POLARIS-calibrated WRF-Hydro with 2 m soil (orange line; labeled
619 with (ii)), and POLARIS-calibrated WRF-Hydro with 40 cm soil (red line; labeled with (iii)) at three
620 selected stations (Gages 11169800, 11157500, and 11152000). NSEs of the simulations are shown. (b),
621 (d), and (f) show the scatter plots of experiment (i) (blue circles), (ii) (orange squares), and (iii) (red
622 triangles) along the x-axis versus the observations along the y-axis. The 1:1 line is shown as black solid
623 line in (b), (d) and (f).

624

625

626 **5. Conclusions and discussions**

627 In this study, we use open access soil databases to inform the parameters in two calibration
628 experiments in WRF-Hydro. We not only create a simulated soil moisture product that outperforms four
629 well-established soil moisture products but we also significantly improve model streamflow fidelity. In
630 our first experiment (i.e., POLARIS-calibrated WRF-Hydro), we replace the soil hydraulic parameters in
631 the default version of WRF-Hydro with the POLARIS-based soil parameters to calibrate surface soil
632 moisture simulations. We evaluate the POLARIS-calibrated WRF-Hydro simulated soil moisture over an
633 8-month period against seven in-situ soil moisture stations and see an improvement across all seven
634 stations after the calibration. On average, KGE increases ~25% after calibration. Compared to other
635 spatially-distributed soil moisture simulations in SMAP L4, NLDAS-2 Noah, VIC, and Mosaic LSMs, the
636 POLARIS-calibrated WRF-Hydro has the best average performance across seven sites and produces the
637 highest correlation, lowest error, and highest KGE in most cases. Despite the improved surface soil
638 moisture fidelity in POLARIS-calibrated WRF-Hydro, streamflow simulation is only moderately
639 improved. As such, we reduce the soil thickness from 2 m in POLARIS-calibrated WRF-Hydro to 40 cm
640 based on SSURGO depth-to-bedrock data to better replicate the effects of the entire soil column on
641 streamflow production in California. Streamflow fidelity significantly improves in our POLARIS-
642 calibrated with 40 cm soil experiment - seven of the nine USGS gages see an increased NSE and the
643 mean of NSEs at the seven improved gages reaches 0.63. Our data-informed calibration method uses open
644 access, spatially-distributed soil physical information available over the CONUS to constrain our
645 hydrological model's parameter uncertainties. Our calibration method does not require iterative model
646 simulations which highlights its simplicity and potentially wide applicability to improve soil moisture and
647 streamflow simulations in fully-distributed hydrological models, which could facilitate studies in a wide
648 range of disciplines in data-scarce areas.

649 Despite the generally high model fidelity, we note that there are still considerable differences between
650 WRF-Hydro soil moisture simulations and the observations at some stations. Consistent with other
651 studies, we are able to explain a large portion of the uncertainties in our soil moisture simulations with the
652 uncertainties of precipitation forcing (Alfieri et al. 2012; Hapuarachchi et al. 2011). The gauge-corrected
653 MRMS precipitation we use in this study is found to substantially deviate from the in-situ precipitation at
654 stations sld and gry, which largely explains the differences between the soil moisture simulation and
655 observation at these locations (Section 4.2). Despite the uncertainties in the gauge-corrected MRMS, it

provides gridded precipitation at high spatial (1 km) and temporal (hourly) resolutions, making it a valuable forcing for high-resolution hydrological models. More details regarding MRMS uncertainties can be found in the Appendix A of Li et al. (2022). Additional uncertainties can be traced to the soil parameters. By using the POLARIS dataset, an observation-based statistical soil property dataset with higher accuracy and spatial resolution, we have constrained some of the parameter uncertainties of soil porosity and saturated hydraulic conductivity. Nevertheless, the performance of our calibrated model is negatively affected by dry-season simulations as we discussed in Section 4.2. Specifically, POLARIS-calibrated WRF-Hydro tends to underestimate the speed of water drainage during the transition period from the wet to dry season (Figs. 5&6). Among various factors that could cause the model's underestimation of drainage speed, the parameter b_{exp} that controls the speed of flows through the soil column is likely the main cause. To derive b , we use the clay fraction from POLARIS and a linear regression model from Cosby et al. (1984), which may result in the propagation and accumulation of uncertainties. Indeed, Cosby et al. (1984) also documented the uncertainties of the calculated b coefficient. From the perspective of flooding and landslide hazard assessment and control, simulation during wet season is of particular importance. For drought monitoring, agriculture, and water resource management, however, dry-season soil moisture simulation is also critical. To improve dry-season soil moisture simulations in WRF-Hydro, the uncertainties of b_{exp} also need to be considered when implementing the calibration method.

In addition to prediction uncertainties, the differences between simulation and observation could originate from other factors including the comparison approach and the possible instrumental errors in soil moisture measurements. To compare with point-scale observations, we use the soil moisture simulated at the grid point that is located closest to the in-situ site. In addition, the WRF-Hydro surface soil moisture is a depth average of the 0–10 cm soil layer while the in-situ soil moisture is measured at 10 cm depth for PSL stations and 5 cm depth for WRCC stations. We also note that the observations might be subject to errors. For example, the observed soil moisture at station lgs was abnormally high during the wet season, exceeding 60%. However, the maximum surface porosity in proximity of station lgs only achieves 0.55 according to the 30-m POLARIS. By referring to the soil moisture sensor instruction manual and consulting with the experts that operate and maintain the PSL stations, we found that the soil moisture sensor at station lgs was likely submerged in ponded water due to the large amount of accumulated precipitation during the wet season and the soil moisture was likely substantially overestimated (Fig. 5b).

To enhance the capability of WRF-Hydro to simulate soil moisture, the utility of POLARIS dataset can be further explored. In addition to median values, POLARIS also provides a range of soil property

statistics including the mean, mode, 5P, and 95P, which can facilitate an investigation on parameter uncertainties in WRF-Hydro associated with individual parameters. In addition, due to a lack of in-situ soil moisture data of deeper soils, this study is focused on calibrating and validating the surface soil moisture. Accurate surface soil moisture is most important for predicting the occurrence of flooding events via a control on rainfall partitioning (Aubert et al. 2003; Crow et al. 2018; Houser et al. 2003; Kerr 2007) and it also provides initial conditions for slope instability models to predict slope failures (Cai et al. 2019; Di Matteo et al. 2018). Nevertheless, soil water content of deeper soils is critical for ecology, agriculture, drought monitoring, and water and energy fluxes. Both the soil parameters in POLARIS and the soil moisture simulations from WRF-Hydro have multiple soil layers that extend to as deep as 2 m below ground, and different parameter values can be assigned to different layers in WRF-Hydro. To calibrate the soil moisture for all soil layers in WRF-Hydro, POLARIS soil properties from other soil layers will also be needed.

Compared to soil moisture, streamflow is the variable that has been more extensively calibrated and used in WRF-Hydro (Lahmers et al. 2019; Wang et al. 2019) which makes the implication of calibrating soil moisture on streamflow simulation an important topic to cover. Our results show that by just calibrating the surface soil moisture the correlation increases and some biases are reduced but streamflow simulation is not significantly improved (Fig. 8). In contrast, in the experiment that adjusts the total soil thickness according to SSURGO, streamflow simulations across most gages are much improved without diminishing the soil moisture model fidelity. This indicates that the 2 m soil column in the default setting of WRF-Hydro largely overestimates the soil thickness in our model domain (Supplemental Fig. 3) and adjusting the total soil thickness is more efficient than calibrating surface soil moisture to improve streamflow fidelity. This is further proved by running an additional experiment, i.e., default WRF-Hydro with 40 cm soil, in which we find the POLARIS-calibrated WRF-Hydro with 40 cm soil still yields the best results on average and default WRF-Hydro with 40 cm soil yields the second best in terms of streamflow simulation (Supplemental Table 5). Compared to other streamflow calibration studies which focus on variables that control the discharge volume and hydrograph shape, such as the water retention depth coefficient (*REFKDT*), bottom openness (*SLOPE*), and Manning's coefficient (*n*), our method is only focused on soil-related parameters and we are able to achieve similar model performance to simulate streamflow (Wang et al. 2019; Yucel et al. 2015). Nevertheless, we acknowledge that applying a spatially homogeneous total soil thickness to a large domain can introduce bias in the simulation of discharge magnitude at some locations (e.g., Gages 11152050 and 11152000) but the current version of WRF-Hydro is not capable of assigning spatially-distributed total soil thickness. Model developments to enable spatially-varying soil thickness would therefore be advantageous. In addition, the frequent and widespread wildfires in the Coast Ranges of central California and their impacts on downstream

723 hydrology have added additional complexities for streamflow predictions (Li et al. 2022). Accordingly,
724 we suggest users consider many factors to replicate the real-world conditions before intensively
725 calibrating the streamflow parameters to avoid overfitting.

726 Given the simplicity of the concept underlying our data-informed calibration method, we argue for its
727 extendibility to other hydrological models that deal with spatially-distributed soil parameters and other
728 geographic areas. Indeed, the applicability of our method to other geographic locations is only limited by
729 the availability of reliable and updated soil hydraulic parameter data. Over the CONUS, POLARIS and
730 SSURGO are open access databases, and for studies outside the U.S., the Global Soil Dataset, for
731 example, provides gridded soil hydraulic parameters for use in Earth Systems Models around the globe
732 (Shangguan et al. 2014).

733

734 **Financial support**

735 This research has been supported by the National Science Foundation (grant no. 1848683).

736 **Data availability statement**

737 The NLDAS-2 reanalysis forcing data are publicly available at NASA GES DISC:
738 <https://doi.org/10.5067/6J5LHHOHZHN4> (Xia et al., 2009). The MRMS gauge-corrected precipitation
739 estimate is archived at <https://mtarchive.geol.iastate.edu/>. POLARIS dataset can be downloaded at
740 <http://hydrology.cee.duke.edu/POLARIS/PROPERTIES/v1.0/> (Chaney et al. 2016). SSURGO dataset is
741 available at <https://websoilsurvey.nrcs.usda.gov/> (Soil Survey Staff, 2021). The PSL in situ soil moisture
742 data are publicly available at <https://psl.noaa.gov/data/obs/datadisplay/> (NOAA PSL, 2021). WRCC soil
743 moisture data is available at <https://wrcc.dri.edu/weather/index.html> (WRCC 2021). SMAP Level 4
744 version 6 soil moisture data is available at <https://nsidc.org/data/spl4smau VERSIONS/6> (Reichle et al. 2021).
745 A more recent version (version 7) of SMAP Level 4 is available at
746 <https://nsidc.org/data/spl4smau VERSIONS/7> (Reichle et al. 2022). NLDAS-2 Noah, VIC, and Mosaic soil
747 moisture datasets are available at
748 <https://disc.gsfc.nasa.gov/datasets?keywords=NLDAS&page=1&measurement=Soil%20Moisture%2FWater%20Content> (NCEP/EMC, 2009, 2012, 2014; Xia et al. 2012). The USGS streamflow is publicly
749 available at <https://doi.org/10.5066/F7P55KJN> (USGS, 2016). All processed data required to reproduce
750 the results of this study are archived on Zenodo at <https://doi.org/10.5281/zenodo.7487179> (Li 2022).

752

753

754

755 **References**

- 756 Acharya S, Kaplan DA, McLaughlin DL, Cohen MJ (2022) In-Situ Quantification and Prediction of
757 Water Yield From Southern US Pine Forests 58:e2021WR031020
758 doi:<https://doi.org/10.1029/2021WR031020>
- 759 Al-Yaari A et al. (2017) Evaluating soil moisture retrievals from ESA's SMOS and NASA's SMAP
760 brightness temperature datasets 193:257-273
- 761 Alfieri L, Salamon P, Pappenberger F, Wetterhall F, Thielen J (2012) Operational early warning systems
762 for water-related hazards in Europe Environmental Science & Policy 21:35-49
763 doi:<https://doi.org/10.1016/j.envsci.2012.01.008>
- 764 Alvioli M, Baum RLJEM, Software (2016) Parallelization of the TRIGRS model for rainfall-induced
765 landslides using the message passing interface 81:122-135
- 766 Aubert D, Loumagne C, Oudin LJJoh (2003) Sequential assimilation of soil moisture and streamflow data
767 in a conceptual rainfall–runoff model 280:145-161
- 768 Baum RL, Savage WZ, Godt JW (2008) TRIGRS: a Fortran program for transient rainfall infiltration and
769 grid-based regional slope-stability analysis, version 2.0. US Geological Survey Reston, VA, USA,
- 770 Becker R, Koppa A, Schulz S, Usman M, aus der Beek T, Schüth C (2019) Spatially distributed model
771 calibration of a highly managed hydrological system using remote sensing-derived ET data Journal of
772 Hydrology 577:123944 doi:<https://doi.org/10.1016/j.jhydrol.2019.123944>
- 773 Berg A, Sheffield J (2018) Climate Change and Drought: the Soil Moisture Perspective Current Climate
774 Change Reports 4:180-191 doi:10.1007/s40641-018-0095-0
- 775 Boucher MA, Quilty J, Adamowski JJWRR (2020) Data assimilation for streamflow forecasting using
776 extreme learning machines and multilayer perceptrons 56:e2019WR026226
- 777 Cai J-S, Jim Yeh T-C, Yan EC, Tang R-X, Hao Y-H, Huang S-Y, Wen J-C (2019) Importance of
778 variability in initial soil moisture and rainfalls on slope stability Journal of Hydrology 571:265-278
779 doi:<https://doi.org/10.1016/j.jhydrol.2019.01.046>
- 780 Campbell Scientific, INC. CS616 and CS625 water content reflectometer instruction manual. Retrieved
781 on Feb. 2021 from <https://psl.noaa.gov/data/obs/instruments/SoilWaterContent.pdf>
- 782 Campbell Scientific, INC. CS615 water content reflectometer instruction manual. Retrieved Feb. 2021.
783 <https://s.campbellsci.com/documents/us/manuals/cs615.pdf>
- 784 Carrão H, Russo S, Sepulcre-Canto G, Barbosa P (2016) An empirical standardized soil moisture index
785 for agricultural drought assessment from remotely sensed data International Journal of Applied Earth
786 Observation and Geoinformation 48:74-84 doi:<https://doi.org/10.1016/j.jag.2015.06.011>

- 787 Chaney NW, Wood EF, McBratney AB, Hempel JW, Nauman TW, Brungard CW, Odgers NP (2016)
788 POLARIS: A 30-meter probabilistic soil series map of the contiguous United States Geoderma
789 274:54-67 doi:10.1016/j.geoderma.2016.03.025
- 790 Chen F, Crow WT, Bindlish R, Colliander A, Burgin MS, Asanuma J, Aida KJRSOE (2018) Global-scale
791 evaluation of SMAP, SMOS and ASCAT soil moisture products using triple collocation 214:1-13
- 792 Coe JA, Kinner DA, Godt JW (2008) Initiation conditions for debris flows generated by runoff at Chalk
793 Cliffs, central Colorado Geomorphology 96:270-297
794 doi:<https://doi.org/10.1016/j.geomorph.2007.03.017>
- 795 Colby B (1956) Relationship of sediment discharge to streamflow. US Dept. of the Interior, Geological
796 Survey, Water Resources Division,
- 797 Cosby, B. J., Hornberger, G. M., Clapp, R. B., and Ginn, T. R.: A Statistical Exploration of the
798 Relationships of Soil Moisture Characteristics to the Physical Properties of Soils, Water Resour. Res.,
799 20(6), 682-690, doi:<https://doi.org/10.1029/WR020i006p00682>, 1984.
- 800 Crow W, Kumar S, Bolten JJH, Sciences ES (2012) On the utility of land surface models for agricultural
801 drought monitoring 16:3451-3460
- 802 Crow W, Van den Berg MJWRR (2010) An improved approach for estimating observation and model
803 error parameters in soil moisture data assimilation 46
- 804 Crow WT, Chen F, Reichle RH, Xia Y, Liu Q (2018) Exploiting Soil Moisture, Precipitation, and
805 Streamflow Observations to Evaluate Soil Moisture/Runoff Coupling in Land Surface Models
806 Geophys Res Lett 45:4869-4878 doi:<https://doi.org/10.1029/2018GL077193>
- 807 Davy P, Lague DJoGRES (2009) Fluvial erosion/transport equation of landscape evolution models
808 revisited 114
- 809 De Santis D, Biondi D, Crow W, Camici S, Modanesi S, Brocca L, Massari CJWRR (2021) Assimilation
810 of satellite soil moisture products for river flow prediction: An extensive experiment in over 700
811 catchments throughout Europe 57:e2021WR029643
- 812 Di Matteo L et al. (2018) Reliability of water content estimation by profile probe and its effect on slope
813 stability Landslides 15:173-180 doi:10.1007/s10346-017-0895-7
- 814 Dottori F, Salamon P, Bianchi A, Alfieri L, Hirpa FA, Feyen LJAwr (2016) Development and evaluation
815 of a framework for global flood hazard mapping 94:87-102
- 816 Douville H, Chauvin F (2000) Relevance of soil moisture for seasonal climate predictions: A preliminary
817 study vol 16.
- 818 Fan X, Liu Y, Gan G, Wu G (2020) SMAP underestimates soil moisture in vegetation-disturbed areas
819 primarily as a result of biased surface temperature data Remote Sensing of Environment 247:111914
820 doi:10.1016/j.rse.2020.111914

- 821 Fennessy MJ, Shukla J (1999) Impact of Initial Soil Wetness on Seasonal Atmospheric Prediction J
822 Climate 12:3167-3180 doi:10.1175/1520-0442(1999)012<3167:IOISWO>2.0.CO;2
- 823 Ford TW, Quiring SM (2019) Comparison of Contemporary In Situ, Model, and Satellite Remote Sensing
824 Soil Moisture With a Focus on Drought Monitoring 55:1565-1582
825 doi:<https://doi.org/10.1029/2018WR024039>
- 826 Friend AD, Kiang NYJJoC (2005) Land surface model development for the GISS GCM: Effects of
827 improved canopy physiology on simulated climate 18:2883-2902
- 828 Gallagher M, Doherty JJEM, Software (2007) Parameter estimation and uncertainty analysis for a
829 watershed model 22:1000-1020
- 830 Gasmo JM, Rahardjo H, Leong EC (2000) Infiltration effects on stability of a residual soil slope
831 Computers and Geotechnics 26:145-165 doi:[https://doi.org/10.1016/S0266-352X\(99\)00035-X](https://doi.org/10.1016/S0266-352X(99)00035-X)
- 832 Gochis, D.J., M. Barlage, R. Cabell, M. Casali, A. Dugger, K. FitzGerald, M. McAllister, J. McCreight, A.
833 RafieeiNasab, L. Read, K. Sampson, D. Yates, Y. Zhang (2020). The WRF-Hydro® modeling
834 system technical description, (Version 5.1.1). NCAR Technical Note. 107 pages. Available online at:
835 <https://ral.ucar.edu/sites/default/files/public/WRFHydroV511TechnicalDescription.pdf>.
- 836 Gong G, Wang L, Condon L, Shearman A, Lall UJJotAWRA (2010) A simple framework for
837 incorporating seasonal streamflow forecasts into existing water resource management practices 1
838 46:574-585
- 839 Gupta HV, Kling H, Yilmaz KK, Martinez GF (2009) Decomposition of the mean squared error and NSE
840 performance criteria: Implications for improving hydrological modelling Journal of Hydrology
841 377:80-91 doi:<https://doi.org/10.1016/j.jhydrol.2009.08.003>
- 842 Handwerger AL, Huang M-H, Fielding EJ, Booth AM, Bürgmann R (2019) A shift from drought to
843 extreme rainfall drives a stable landslide to catastrophic failure Scientific Reports 9:1569
844 doi:10.1038/s41598-018-38300-0
- 845 Hapuarachchi HAP, Wang QJ, Pagano TC (2011) A review of advances in flash flood forecasting
846 25:2771-2784 doi:<https://doi.org/10.1002/hyp.8040>
- 847 Holtan, H. N., C. B. England, G. P. Lawless, and G. A. Schumaker, Moisture-tension data for selected
848 soils on experimental watersheds, Rep. ARS 41-144, 609 pp., Agric. Res. Serv., Beltsville, Md., 1968.
- 849 Houser PRJHoW, Climate, Water: Atmospheric Chemistry H, Wiley SIJ, Sons IH, New Jersey (2003)
850 Infiltration and soil moisture processes
- 851 Johnson K, Sitar NJCGJ (1990) Hydrologic conditions leading to debris-flow initiation 27:789-801
- 852 Jong B-T, Ting M, Seager R (2016) El Niño's impact on California precipitation: seasonality, regionality,
853 and El Niño intensity Environmental Research Letters 11:054021 doi:10.1088/1748-
854 9326/11/5/054021

- 855 Kang Y, Khan S, Ma X (2009) Climate change impacts on crop yield, crop water productivity and food
856 security – A review Progress in Natural Science 19:1665-1674
857 doi:<https://doi.org/10.1016/j.pnsc.2009.08.001>
- 858 Kean JW, McCoy SW, Tucker GE, Staley DM, Coe JA (2013) Runoff-generated debris flows:
859 Observations and modeling of surge initiation, magnitude, and frequency Journal of Geophysical
860 Research: Earth Surface 118:2190-2207 doi:<https://doi.org/10.1002/jgrf.20148>
- 861 Kerr YH (2007) Soil moisture from space: Where are we? Hydrogeology Journal 15:117-120
862 doi:[10.1007/s10040-006-0095-3](https://doi.org/10.1007/s10040-006-0095-3)
- 863 Kling H, Fuchs M, Paulin M (2012) Runoff conditions in the upper Danube basin under an ensemble of
864 climate change scenarios Journal of Hydrology 424-425:264-277
865 doi:<https://doi.org/10.1016/j.jhydrol.2012.01.011>
- 866 Koster RD (2004) Realistic initialization of land surface states: Impacts on subseasonal forecast skill vol
867 5.
- 868 Koster RD, Guo Z, Yang R, Dirmeyer PA, Mitchell K, Puma MJ (2009) On the Nature of Soil Moisture
869 in Land Surface Models J Climate 22:4322-4335 doi:[10.1175/2009JCLI2832.1](https://doi.org/10.1175/2009JCLI2832.1)
- 870 Koster RD et al. (2010) Contribution of land surface initialization to subseasonal forecast skill: First
871 results from a multi-model experiment 37
- 872 Kumar SV, Dirmeyer PA, Peters-Lidard CD, Bindlish R, Bolten JJRSOE (2018) Information theoretic
873 evaluation of satellite soil moisture retrievals 204:392-400
- 874 Lahmers TM, Castro CL, Hazenberg P (2020) Effects of Lateral Flow on the Convective Environment in
875 a Coupled Hydrometeorological Modeling System in a Semiarid Environment J Hydrometeor 21:615-
876 642 doi:[10.1175/JHM-D-19-0100.1](https://doi.org/10.1175/JHM-D-19-0100.1)
- 877 Lahmers TM et al. (2019) Enhancing the structure of the WRF-Hydro hydrologic model for semiarid
878 environments 20:691-714
- 879 Lahmers, T. M., Kumar, S. V., Rosen, D., Dugger, A., Gochis, D. J., Santanello, J. A., et al. (2022).
880 Assimilation of NASA's Airborne Snow Observatory snow measurements for improved hydrological
881 modeling: A case study enabled by the coupled LIS/WRF-Hydro system. Water Resources Research,
882 58, e2021WR029867. <https://doi.org/10.1029/2021WR029867>
- 883 Leach JM, Kornelsen KC, Coulibaly PJJoH (2018) Assimilation of near-real time data products into
884 models of an urban basin 563:51-64
- 885 Lee H, Seo D-J, Koren V (2011) Assimilation of streamflow and in situ soil moisture data into
886 operational distributed hydrologic models: Effects of uncertainties in the data and initial model soil
887 moisture states Adv Water Resour 34:1597-1615 doi:<https://doi.org/10.1016/j.advwatres.2011.08.012>

- 888 Legates DR, Mahmood R, Levia DF, DeLiberty TL, Quiring SM, Houser C, Nelson FEJPiPG (2011) Soil
889 moisture: A central and unifying theme in physical geography 35:65-86
- 890 Li C et al. (2022) Augmentation of WRF-Hydro to simulate overland-flow- and streamflow-generated
891 debris flow susceptibility in burn scars Nat Hazards Earth Syst Sci 22:2317-2345 doi:10.5194/nhess-
892 22-2317-2022
- 893 Li C (2022) data-informed calibration of WRF-Hydro data1. Zenodo, [Data set]. doi:
894 <https://doi.org/10.5281/zenodo.7487179>
- 895 Loizu J, Massari C, Alvarez-Mozos J, Tarpanelli A, Brocca L, Casali JJAiWR (2018) On the assimilation
896 set-up of ASCAT soil moisture data for improving streamflow catchment simulation 111:86-104
- 897 Ma H, Zeng J, Chen N, Zhang X, Cosh MH, Wang W (2019) Satellite surface soil moisture from SMAP,
898 SMOS, AMSR2 and ESA CCI: A comprehensive assessment using global ground-based observations
899 Remote Sensing of Environment 231:111215 doi:<https://doi.org/10.1016/j.rse.2019.111215>
- 900 Massari C, Brocca L, Moramarco T, Tramblay Y, Lescot J-FDJAiWR (2014) Potential of soil moisture
901 observations in flood modelling: Estimating initial conditions and correcting rainfall 74:44-53
- 902 Matgen P et al. (2010) Towards the sequential assimilation of SAR-derived water stages into hydraulic
903 models using the Particle Filter: proof of concept 14:1773-1785
- 904 Mohanty BP, Cosh MH, Lakshmi V, Montzka C (2017) Soil Moisture Remote Sensing: State-of-the-
905 Science 16:vzj2016.2010.0105 doi:<https://doi.org/10.2136/vzj2016.10.0105>
- 906 Narasimhan B, Srinivasan R (2005) Development and evaluation of Soil Moisture Deficit Index (SMDI)
907 and Evapotranspiration Deficit Index (ETDI) for agricultural drought monitoring vol 133.
- 908 Nash JE, Sutcliffe JV (1970) River flow forecasting through conceptual models part I — A discussion of
909 principles Journal of Hydrology 10:282-290 doi:[https://doi.org/10.1016/0022-1694\(70\)90255-6](https://doi.org/10.1016/0022-1694(70)90255-6)
- 910 NCEP/EMC (2012), NLDAS Noah Land Surface Model L4 Hourly 0.125 x 0.125 degree V002, Edited
911 by David Mocko, NASA/GSFC/HSL, Greenbelt, Maryland, USA, Goddard Earth Sciences Data and
912 Information Services Center (GES DISC), [Data set], Accessed: 12/02/2021,
913 10.5067/47Z13FNQODKV
- 914 NCEP/EMC (2014), NLDAS VIC Land Surface Model L4 Hourly 0.125 x 0.125 degree V002, Edited by
915 David Mocko, NASA/GSFC/HSL, Greenbelt, Maryland, USA, Goddard Earth Sciences Data and
916 Information Services Center (GES DISC), [Data set], Accessed: 12/02/2021,
917 10.5067/ELBDAPAKNGJ9
- 918 NCEP/EMC (2009), NLDAS Mosaic Land Surface Model L4 Hourly 0.125 x 0.125 degree V002, Edited
919 by David Mocko, NASA/GSFC/HSL, Greenbelt, Maryland, USA, Goddard Earth Sciences Data and
920 Information Services Center (GES DISC), [Data set], Accessed: 12/02/2021,
921 10.5067/EN4MBWTCENES5

- 922 Niu G-Y et al. (2011) The community Noah land surface model with multiparameterization options
923 (Noah-MP): 1. Model description and evaluation with local-scale measurements J Geophys Res Atm
924 116 doi:<https://doi.org/10.1029/2010JD015139>
- 925 NOAA Physical Sciences Laboratory (PSL): Surface Meteorology and Physics Data, NOAA [Data set],
926 <https://psl.noaa.gov/data/obs/datadisplay/>, access: 28 June 2021.
- 927 Rawls, W., P. Yates, and L. Asmussen, Calibration of selected infiltration equations for the Georgia
928 Coastal Plain, Rep. USDA-ARS-S113, 110 pp., Agric. Res. Serv., Beltsville, Md., 1976
- 929 Ray RL, Jacobs JM (2007) Relationships among remotely sensed soil moisture, precipitation and
930 landslide events Nat Hazards 43:211-222 doi:10.1007/s11069-006-9095-9
- 931 Reichle, R. H., de Lannoy, G. J. M., Liu, Q., Ardizzone, J. V., Colliander, A., Conaty, A., Crow, W.,
932 Jackson, T. J., Jones, L. A., Kimball, J. S., Koster, R. D., Mahanama, S. P., Smith, E. B., Berg, A.,
933 Bircher, S., Bosch, D., Caldwell, T. G., Cosh, M., González-Zamora, Á., Holifield Collins, C. D.,
934 Jensen, K. H., Livingston, S., Lopez-Baeza, E., Martínez-Fernández, J., McNairn, H., Moghaddam,
935 M., Pacheco, A., Pellarin, T., Prueger, J., Rowlandson, T., Seyfried, M., Starks, P., Su, Z., Thibeault,
936 M., van der Velde, R., Walker, J., Wu, X., & Zeng, Y. (2017). Assessment of the SMAP Level-4
937 surface and root-zone soil moisture product using in situ measurements. Journal of Hydrometeorology,
938 18(10), 2621–2645. <https://doi.org/10.1175/jhm-d-17-0063.1>
- 939 Reichle, R., G. De Lannoy, R. D. Koster, W. T. Crow, J. S. Kimball, and Q. Liu. (2021). SMAP L4
940 Global 3-hourly 9 km EASE-Grid Surface and Root Zone Soil Moisture Analysis Update, Version 6
941 [Data Set]. Boulder, Colorado USA. NASA National Snow and Ice Data Center Distributed Active
942 Archive Center. <https://doi.org/10.5067/6P2EV47VMYPC>. Date Accessed 12-02-2021.
- 943 Reichle, R., G. De Lannoy, R. D. Koster, W. T. Crow, J. S. Kimball, Q. Liu, and M. Bechtold. (2022).
944 SMAP L4 Global 3-hourly 9 km EASE-Grid Surface and Root Zone Soil Moisture Analysis Update,
945 Version 7 [Data Set]. Boulder, Colorado USA. NASA National Snow and Ice Data Center Distributed
946 Active Archive Center. <https://doi.org/10.5067/LWJ6TF5SZRG3>. Date Accessed 12-27-2022.
- 947 Rosenzweig C, Tubiello FN, Goldberg R, Mills E, Bloomfield J (2002) Increased crop damage in the US
948 from excess precipitation under climate change vol 12.
- 949 Schaeefli B, Gupta HV (2007) Do Nash values have value? Hydrological Processes 21:2075-2080
950 doi:<https://doi.org/10.1002/hyp.6825>
- 951 Seneviratne SI et al. (2010) Investigating soil moisture–climate interactions in a changing climate: A
952 review Earth-Science Reviews 99:125-161 doi:<https://doi.org/10.1016/j.earscirev.2010.02.004>
- 953 Seneviratne SI et al. (2013) Impact of soil moisture-climate feedbacks on CMIP5 projections: First results
954 from the GLACE-CMIP5 experiment 40:5212-5217 doi:<https://doi.org/10.1002/grl.50956>

- 955 Shangguan W, Dai Y, Duan Q, Liu B, Yuan H (2014) A global soil data set for earth system modeling
956 6:249-263 doi:<https://doi.org/10.1002/2013MS000293>
- 957 Silver M, Karnieli A, Ginat H, Meiri E, Fredj E (2017) An innovative method for determining
958 hydrological calibration parameters for the WRF-Hydro model in arid regions Environmental
959 Modelling & Software 91:47-69 doi:<https://doi.org/10.1016/j.envsoft.2017.01.010>
- 960 Sofokleous I, Bruggeman A, Camera C, Eliades M (2022) Grid-based calibration of the WRF-Hydro with
961 Noah-MP model with improved groundwater and transpiration process equations Journal of
962 Hydrology:128991 doi:<https://doi.org/10.1016/j.jhydrol.2022.128991>
- 963 Soil Survey Staff, Natural Resources Conservation Service, United States Department of Agriculture.
964 Web Soil Survey [Data set]. Available online at <https://websoilsurvey.nrcs.usda.gov/>. Accessed
965 12/13/2021.
- 966 Sweeney D, Robertson P (1979) A fundamental approach to slope stability problems in Hong Kong.
967 Hong Kong Engineer. October,
- 968 Tang H, McGuire LA, Rengers FK, Kean JW, Staley DM, Smith JBJGRL (2019) Developing and testing
969 physically based triggering thresholds for runoff-generated debris flows 46:8830-8839
- 970 Tavakol A, Rahmani V, Quiring SM, Kumar SV (2019) Evaluation analysis of NASA SMAP L3 and L4
971 and SPoRT-LIS soil moisture data in the United States Remote Sensing of Environment 229:234-246
972 doi:<https://doi.org/10.1016/j.rse.2019.05.006>
- 973 U.S. Geological Survey (USGS) (2016). National Water Information System data, USGS Water Data for
974 the Nation, USGS [Data set], <https://doi.org/10.5066/F7P55KJN>.
- 975 Vergopolan N, Chaney NW, Beck HE, Pan M, Sheffield J, Chan S, Wood EF (2020) Combining hyper-
976 resolution land surface modeling with SMAP brightness temperatures to obtain 30-m soil moisture
977 estimates Remote Sensing of Environment 242:111740 doi:<https://doi.org/10.1016/j.rse.2020.111740>
- 978 Wagner S, Fersch B, Yuan F, Yu Z, Kunstmann HJWRR (2016) Fully coupled atmospheric-hydrological
979 modeling at regional and long-term scales: Development, application, and analysis of WRF-HMS
980 52:3187-3211
- 981 Wang G, Garcia D, Liu Y, de Jeu R, Johannes Dolman A (2012) A three-dimensional gap filling method
982 for large geophysical datasets: Application to global satellite soil moisture observations
983 Environmental Modelling & Software 30:139-142 doi:<https://doi.org/10.1016/j.envsoft.2011.10.015>
- 984 Wang J, Wang C, Rao V, Orr A, Yan E, Kotamarthi R (2019) A parallel workflow implementation for
985 PEST version 13.6 in high-performance computing for WRF-Hydro version 5.0: a case study over the
986 midwestern United States Geosci Model Dev 12:3523-3539 doi:[10.5194/gmd-12-3523-2019](https://doi.org/10.5194/gmd-12-3523-2019)

- 987 Western Regional Climate Center (2021). Current WRCC Weather Data Plots [Data set]. Retrieved from:
988 <https://wrcc.dri.edu/weather/> access: 12/06/2021.
- 989 Xia Y, Ek MB, Wu Y, Ford T, Quiring SM (2015) Comparison of NLDAS-2 Simulated and NASMD
990 Observed Daily Soil Moisture. Part I: Comparison and Analysis J Hydrometeor 16:1962-1980
991 doi:10.1175/JHM-D-14-0096.1
- 992 Xia Y et al. (2012) Continental-scale water and energy flux analysis and validation for North American
993 Land Data Assimilation System project phase 2 (NLDAS-2): 2. Validation of model-simulated
994 streamflow J Geophys Res Atm 117 doi:<https://doi.org/10.1029/2011JD016051>
- 995 Xia Y et al. (2014) Evaluation of multi-model simulated soil moisture in NLDAS-2 Journal of Hydrology
996 512:107-125 doi:<https://doi.org/10.1016/j.jhydrol.2014.02.027>
- 997 Xu L, Abbaszadeh P, Moradkhani H, Chen N, Zhang XJRSOE (2020) Continental drought monitoring
998 using satellite soil moisture, data assimilation and an integrated drought index 250:112028
- 999 Yeh TC, Wetherald RT, Manabe S (1984) The Effect of Soil Moisture on the Short-Term Climate and
1000 Hydrology Change—A Numerical Experiment Mon Weather Rev 112:474-490 doi:10.1175/1520-
1001 0493(1984)112<0474:TEOSMO>2.0.CO;2
- 1002 Yin D, Xue ZG, Gochis DJ, Yu W, Morales M, Rafieeinab A (2020) A Process-Based, Fully
1003 Distributed Soil Erosion and Sediment Transport Model for WRF-Hydro 12:1840
- 1004 Yu G, Wright DB, Li Z (2020) The Upper Tail of Precipitation in Convection-Allowing Regional
1005 Climate Models and Their Utility in Nonstationary Rainfall and Flood Frequency Analysis
1006 8:e2020EF001613 doi:<https://doi.org/10.1029/2020EF001613>
- 1007 Yucel I, Onen A, Yilmaz KK, Gochis DJ (2015) Calibration and evaluation of a flood forecasting system:
1008 Utility of numerical weather prediction model, data assimilation and satellite-based rainfall Journal of
1009 Hydrology 523:49-66 doi:<https://doi.org/10.1016/j.jhydrol.2015.01.042>
- 1010 Yuste J, Baldocchi DD, Gershenson A, Goldstein A, Misson L, Wong S (2007) Microbial soil respiration
1011 and its dependency on carbon inputs, soil temperature, and moisture vol 13.
- 1012 Zhang, J. et al. (2011). National Mosaic and Multi-Sensor QPE (NMQ) system: Description, results, and
1013 future plans. Bull. Amer. Meteor. Soc., 92, 1321–1338, <https://doi.org/10.1175/2011BAMS-D-11-00047.1>.
- 1015 Zhang, J., Qi, Y., Langston, C., Kaney, B., & Howard, K. (2014). A real-time algorithm for merging radar
1016 QPEs with rain gauge observations and orographic precipitation climatology. J. Hydrometeor., 15,
1017 1794–1809, <https://doi.org/10.1175/JHM-D-13-0163.1>.
- 1018 Zhang, J. et al. (2016). Multi-Radar Multi-Sensor (MRMS) quantitative precipitation estimation: Initial
1019 operating capabilities. Bull. Amer. Meteor. Soc., 97, 621–638, <https://doi.org/10.1175/BAMS-D-14-00174.1>.

1021 Zhuo L, Han D, Dai Q, Islam T, Srivastava PK (2015) Appraisal of NLDAS-2 Multi-Model Simulated
1022 Soil Moistures for Hydrological Modelling Water Resources Management 29:3503-3517
1023 doi:10.1007/s11269-015-1011-1
1024